

ATOMIC LINE SPECTRAL FILTERS  
FOR NEODYMIUM LASER  
RECEIVERS

DTIC FILE COPY

(2)

C. S. Liu, P. J. Chantry and C. L. Chen

November 26, 1986

Final Report  
Contract No. N00014-85-C-0035  
Office of Naval Research

DTIC  
ELECTED  
APR 15 1987  
S D

This document has been approved  
for public release and sale; its  
distribution is unlimited



Westinghouse R&D Center  
1310 Beulah Road  
Pittsburgh, Pennsylvania 15235

87 3 26 030

**ATOMIC LINE SPECTRAL FILTERS  
FOR NEODYMIUM LASER  
RECEIVERS**

C. S. Liu, P. J. Chantry and C. L. Chen

November 26, 1986

Final Report  
Contract No. N00014-85-C-0035  
Office of Naval Research



Accession For	
NTIS	CRA&I <input checked="" type="checkbox"/>
DTIC	TAB <input type="checkbox"/>
Unannounced <input type="checkbox"/>	
Justification	
By <i>ltr. on file</i>	
Distribution	
Availability Codes	
Dist	Avail and/or Special
A-1	



Westinghouse R&D Center  
1310 Beulah Road  
Pittsburgh, Pennsylvania 15235

## TABLE OF CONTENTS

	<u>Page</u>
1. INTRODUCTION . . . . .	1
2. THE TlCl SYSTEM . . . . .	4
2.1 Steady State Analysis . . . . .	6
2.2 Input Data . . . . .	13
2.2.1 Absorption Cross Sections . . . . .	13
2.2.2 Quenching Cross Sections . . . . .	14
2.2.3 Reformation Reactions . . . . .	14
2.2.4 Diffusion Rates . . . . .	15
2.3 Calculations . . . . .	15
2.3.1 No Buffer Gas . . . . .	17
2.3.2 With Buffer Gas . . . . .	19
2.3.3 With Extra Chlorine . . . . .	21
2.3.4 With Added Chlorine and Buffer Gas . . .	23
2.3.5 Sensitivity Study . . . . .	25
3. THE Tl-Cs SYSTEM . . . . .	28
3.1 Collisional Transfer Excitation. . . . .	28
3.2 The Experiment . . . . .	31
3.2.1 The Cesium Cell . . . . .	31
3.2.2 Experimental Apparatus . . . . .	33
3.3 852 nm and 894 nm Fluorescence from Pulse Excited Cs( $6P_{1/2}$ ) and Cs( $6P_{3/2}$ ) States . . . . .	36
3.3.1 Experimental Conditions . . . . .	36
3.3.2 Data Acquisition . . . . .	37
3.4 Data Analysis . . . . .	46
3.4.1 Time Dependent Collisional Mixing Model	46
3.4.2 Curve Fitting to $N_1(t)$ and $N_2(t)$ . . . . .	51

3.4.3 The Transport of Resonance Radiation . . . . .	55
3.4.3.1 The Escape Factor, $g$ . . . . .	55
3.4.3.2 The Effective Number of Hyperfine Components, $f_e$ . . . . .	58
3.4.4 Reconciling Computed and Measured Values of $\tau_f$ and $\tau_s$ . . . . .	65
3.5 Pump Power Implications . . . . .	70
4. CONCLUSIONS AND RECOMMENDATIONS . . . . .	74
4.1 The TlCl Based ALF Concept . . . . .	74
4.2 The Cs-Tl Based ALF Concept . . . . .	75
5. REFERENCES . . . . .	78
ACKNOWLEDGEMENTS . . . . .	80

## 1. INTRODUCTION

This report summarizes research work performed at the Westinghouse R&D Center under ONR Contract No. N00014-85-C-0035, "Atomic Line Spectral Filters for Neodymium Laser Receivers," for the period between November 26, 1984 and November 25, 1985. The major efforts of this project were: (1) to reassess the technical merits of a Tl atomic line filter (ALF) employing a low vapor density TlCl and (2) to measure the excited state cesium trapping lifetimes and to derive the self-quenching cross sections of excited state cesium atoms. Tantalum

These two separate efforts address alternative approaches to the implementation of an ALF based on metastable Tl atoms, Tl<sub>m</sub>, whose absorption wavelength (535 nm) matches the frequency doubled Nd:Be<sub>3</sub> laser. The first approach uses photodissociation to produce Tl<sub>m</sub> directly from TlCl. The second approach involves resonantly pumping the Cs in a Tl-Cs mixture and collisionally transferring energy to the Tl to sustain the required density of Tl<sub>m</sub>.

Previous experimental work by Liu (1985) on the first approach confirmed the general viability of the scheme, but at the TlCl densities used ( $2 \times 10^{13} - 6 \times 10^{15} / \text{cm}^3$ ) the metastable lifetime was found to be controlled by collisional quenching by the TlCl molecules. An important conclusion from the work was that a TlCl based filter would need to be operated at lower TlCl densities. Consequently, the medium would be optically thin to the pumping light, and one might expect an optimum density to exist. The objective of the modelling calculations reported in Section 2 was to explore this concept and establish where in parameter space the optimum operating point is likely to lie. In the analysis we have attempted to include all the processes which might be conceivably important in determining the sustainable Tl<sub>m</sub> density, and to track the densities of all the products. Of particular interest is the

density of ground state thallium,  $Tl_o$ , resulting directly from photodissociation or from quenching of the  $Tl_m$ . This species is expected to react with the available Cl or  $Cl_2$  to reform  $TlCl$ . Under many of the conditions considered the primary reformation reaction is with Cl, at the wall. This implies a degree of coverage of the surface with condensed Tl, which must be kept sufficiently low that it does not affect the optical properties of the windows. The coverage is determined by the balance between the rate of condensation of the Tl and its chemical ablation by the Cl atoms. It will therefore be a decreasing function of temperature, and an increasing function of  $[Tl_o]$ , the steady state volume concentration of ground state thallium atoms. The prescribed density of  $TlCl$  sets a lower bound to the temperature, and this will probably be sufficient to maintain a suitably low coverage of Tl. An upper bound on the required temperature will be the dew point of Tl corresponding to the calculated value of  $[Tl_o]$ . In any case the potential problem of Tl condensation is best mitigated by choosing conditions which do not imply excessively large values of  $[Tl_o]$ . To this end, we explore the possible advantage of adding chlorine to the material mix, as a method of accelerating the reformation of  $TlCl$  from  $Tl_o$  and  $Cl_2$  via a gas phase reaction.

The results indicate that for  $TlCl$  vapor densities below  $10^{13} \text{ cm}^{-3}$  a  $Tl_m$  density of  $10^{10} \text{ cm}^{-3}$  can be sustained by a pump power density of  $100 \text{ mW/cm}^2$ . This power could be easily provided by a mercury 254 nm resonance lamp. The required input data to the model are, however, incomplete and we recognize that the conclusions are therefore correspondingly uncertain. The effects of order-of-magnitude changes in the various input parameters is explored in order to convincingly identify the more important processes. Thus the calculations identify the approximate region where operation of such a filter will be optimized, and thereby will improve the focus of future experiments bearing on this approach.

In Section 3 we describe the design, performance and analysis of an experiment to measure the effective lifetime of Cs atoms resonantly

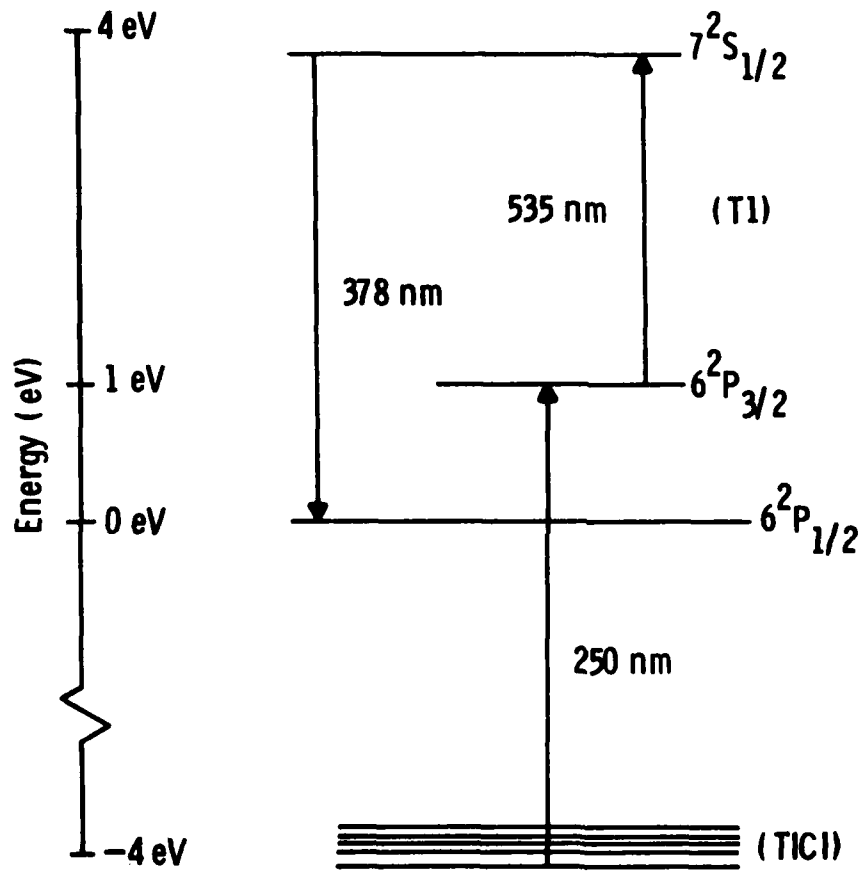
pumped to the  $6P_{1/2}$  or the  $6P_{3/2}$  states in pure cesium. This lifetime is important in determining the pump power requirements of a Tl-Cs ALF, and therefore the experiment described is an essential first step in demonstrating the feasibility of such a device. It was anticipated from the outset that the two Cs excited states would be collisionally mixed, and that their effective lifetime would be determined by the effects of radiation trapping. In general the latter effect is enhanced by increased density, up to the region where collisional broadening of the lines becomes dominant. In order to quantify this behavior the experiments were performed over a wide range of Cs densities,  $\sim 10^{11} \text{ cm}^{-3}$  to  $\sim 2 \times 10^{14} \text{ cm}^{-3}$ . In the analysis of the data we find it necessary to include the effects of the hyperfine structure of the lines on the radiation trapping, and to invoke a surprisingly large cross section for collisional self quenching. The presence of this unanticipated loss process causes the effective lifetime of the  $\text{Cs}^*$  to have a maximum value of  $\sim 35 \mu\text{s}$  occurring at a Cs density of  $\sim 2 \times 10^{13} \text{ cm}^{-3}$  in the present apparatus. In the absence of collisional quenching the lifetime would reach  $80 \mu\text{s}$ . The lower value achieved is nevertheless adequate for a viable Cs-Tl ALF.

Section 4 of this report discusses the conclusions to be drawn from this work, and the resulting recommendations for subsequent work directed towards the ultimate goal of demonstrating a viable ALF based on Tl<sub>m</sub>, and providing the data base required to properly optimise its final design.

## 2. THE TlCl SYSTEM

A simplified energy level diagram of thallium chloride and thallium is shown in Figure 2.1. An active thallium ALF with dissociative excitation of TlCl requires two photon absorption processes. Initially, the metastable state of Tl is populated by a 250 nm pump source. The absorption of a 535 nm photon from a laser transmitter is ultimately detected via the emission of a 378 nm photon from the Tl( $^2S_{1/2}$ ) state. The results of previous studies (Liu et al., 1985) on Tl atomic line filters using TlCl indicated that the pump power at 250 nm required for photodissociative excitation increases with the TlCl vapor density due to a large collisional quenching cross section of Tl( $^2P_{3/2}$ ) atoms by TlCl molecules. In order to reduce the pump power, we have explored the possibility of using very low TlCl vapor density. One conclusion from the study was that the optimal conditions for a TlCl based filter would involve lower TlCl vapor density from  $10^{15}/\text{cm}^3$  to below  $10^{13}/\text{cm}^3$ . Loss of metastables by diffusion to the walls could be prevented by addition of a buffer gas. Starting from this modified concept of how to implement this particular atomic line filter we performed the modeling calculations. We have attempted to include in the calculations all conceivably important processes. The required data is, however, incomplete and we recognize from the outset that our conclusions carry a corresponding uncertainty. Nevertheless, it fulfills the primary objective of this study, namely to identify the approximate region of parameter space where operation of such a filter will be optimized. Exploration of this region in future experiments should then be able to remove the uncertainties inherent in the present calculations.

Dwg. 9378A95



Energy level diagram of TlCl and Tl

Figure 2.1 Energy level diagram of TlCl and Tl.

## 2.1 STEADY STATE ANALYSIS

In designing a thallium atomic line filter the quantities of primary importance are: (1) the achievable density of the thallium metastables  $Tl_m$  ( $=[Tl_m]$ ), (2) the required pumping photon flux density ( $=N_p$ ), and (3) the operating temperature required to keep all the active species in the gaseous state. In this analysis, all conceivable reactions which might affect these quantities are taken into account. They are listed in Table 2.1 as Eqs. (2.1) to (2.11) and in each case the relevant reaction cross section or rate coefficient is indicated. In addition, we include the effects of diffusion of  $Tl_m$ ,  $Tl_o$ , and Cl to the walls of the container, where  $Tl_m$  is assumed to be quenched with probability  $p_m$ , and  $Tl_o$  and Cl are assumed to stick with probabilities  $p_1$  and  $p_2$ . Under steady state conditions  $Tl_o$  and Cl stick at equal rates, and leave as  $TlCl$  at the same rate.

The complete set of reactions is represented schematically in Figure 2.2. For the purpose of this analysis, it is assumed that the steady state spatial distributions of the relevant species are adequately represented by the fundamental diffusion mode of the container, modified by the particle reflection at the physical boundaries. With this assumption we may, in general, represent the local diffusion loss rate of species  $n_i$  by

$$\frac{d[n_i]}{dt} = - \frac{D_i[n_i]}{\Lambda_i^2}$$

$$= - d_i[n_i] \quad (2.12)$$

where

$$d_i = \frac{D_i}{\Lambda_i^2} \quad (2.13)$$

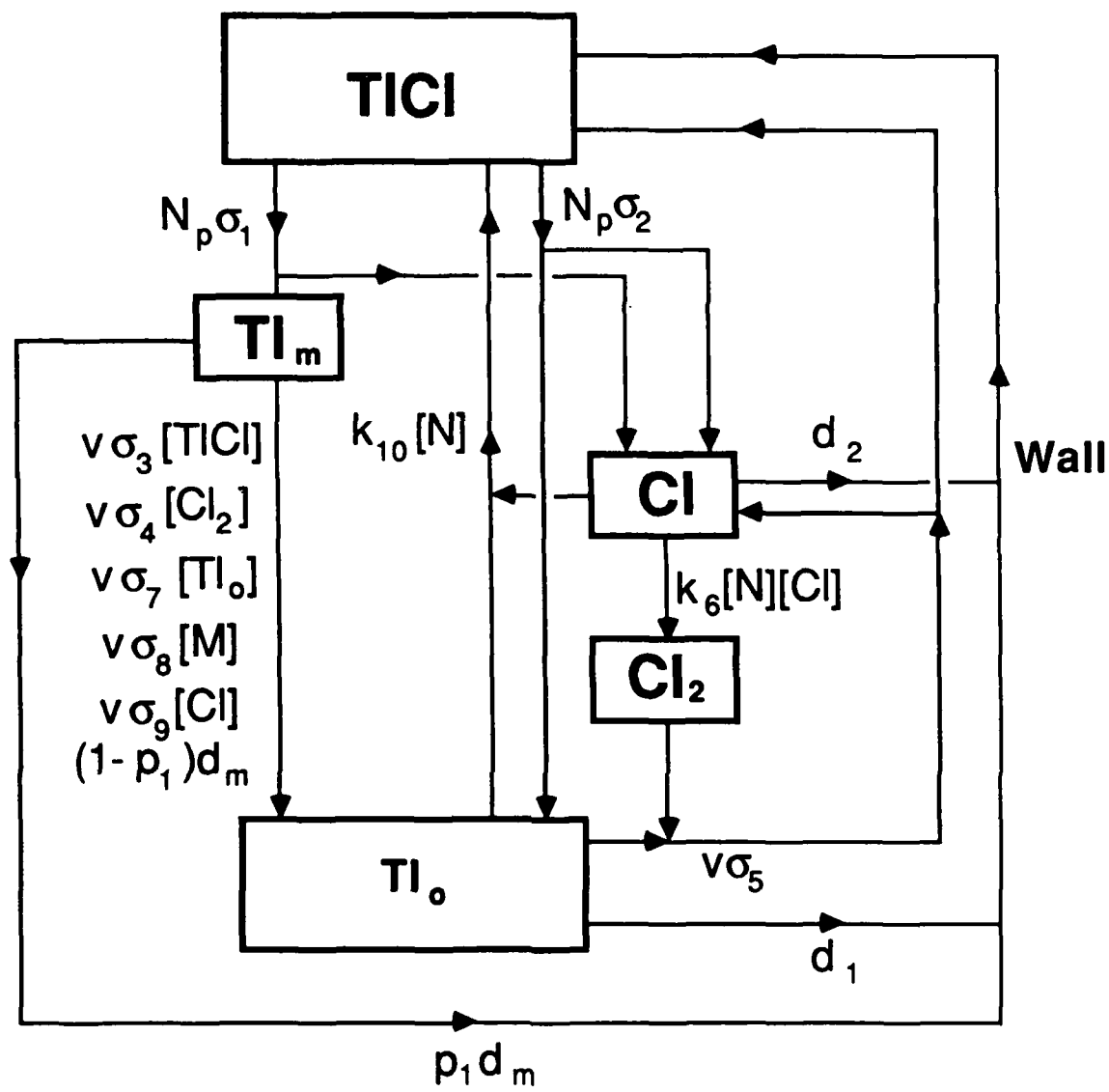
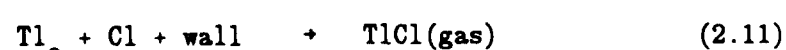
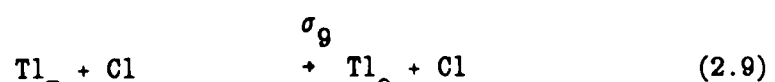
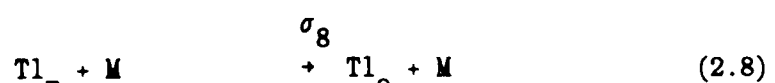
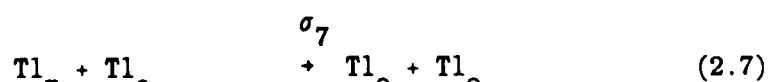
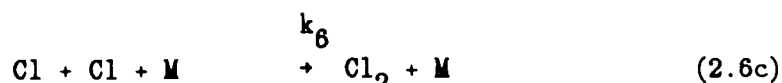
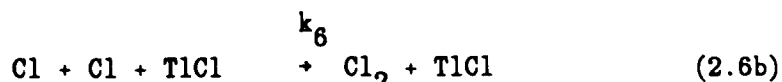
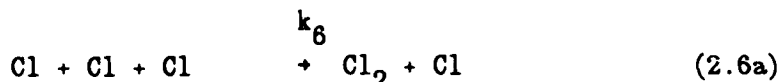
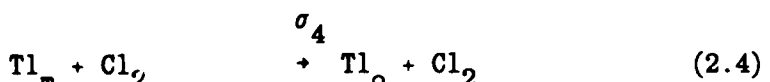
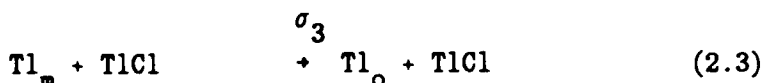


Figure 2.2 Reaction scheme for sustaining a density of  $Tl_m$  by photodissociation of  $TlCl$ .

Table 2.1 Reactions involved in sustaining a Tl density by photo-dissociation of TlCl. See also Figure 2.2



In these equations  $D_i$  is the diffusion coefficient of particles  $n_i$ , assumed to be independent of position, and  $\Lambda_i$  is the effective fundamental mode diffusion length of the container. In calculating  $\Lambda_i$  account must be taken of the non-zero particle density at the walls. At high densities of scatterers,  $N$ , and provided the sticking probability  $p_i$  is close to unity, then  $\Lambda_i$  differs little from the conventional value  $\Lambda_o$ . In the present problem neither assumption is necessarily valid. In this situation it is appropriate to employ a boundary condition involving the concept of a "linear extrapolation distance,"  $\lambda_i$ , whose inverse is the logarithmic gradient of the particle density at the wall:

$$\frac{1}{n_i} \cdot \frac{dn_i}{dq} \Big|_{\text{wall}} = -\frac{1}{\lambda_i} \quad (2.14)$$

The definition of  $\lambda_i$  in terms of the diffusion mean free path (or equivalently the diffusion coefficient  $D_i$ ), and the sticking probability  $p_i$  has been discussed in detail elsewhere (Chantry, 1985). For the present purposes we employ the empirical analytical approximation

$$\frac{1}{\Lambda_i^2} = \frac{1}{\Lambda_o^2 + l_o \lambda_i} \quad (2.15)$$

where  $\Lambda_o$  is the container diffusion length computed in the conventional way, i.e. with the assumption that  $n_i(\text{wall}) = 0$ , and  $l_o$  is the container volume to surface area ratio. For the cylindrical containers of present interest these quantities are given by

$$\frac{1}{\Lambda_o^2} = \left(\frac{\pi}{h_o}\right)^2 + \left(\frac{2.405}{r_o}\right)^2 \quad (2.16)$$

$$\frac{1}{l_o} = \frac{2}{h_o} + \frac{2}{r_o} \quad (2.17)$$

and

$$\frac{1}{\lambda_i} = \frac{p_i}{2(2-p_i)} \frac{Nv}{(D_i N)} \quad (2.18)$$

Use of Eqs. (2.15) through (2.18) is expected to give values of  $A_i$  accurate to 10% or better. In view of the other uncertainties in the present analysis this degree of accuracy is considered acceptable. Use of Eq. (2.15) avoids the need to solve iteratively the transcendental equations involved in a case by case application of Eq. (2.14).

In the following analysis we shall use the subscripts  $i = m, 1,$  and 2 to denote quantities representative of species  $Tl_m$ ,  $Tl_o$ , and  $Cl$  respectively. For the time being we represent their respective local diffusion loss frequencies by  $d_m$ ,  $d_1$ , and  $d_2$ , with the understanding that their values are quantitatively determined by Eq. (2.13), and (2.15) through (2.18).

In developing steady state solutions to Eqs. (2.1) to (2.10) we adopt the viewpoint that the pumping photon flux  $N_p$ , and densities  $[TlCl]$ ,  $[Cl_2]$ , and  $[M]$  (where  $M$  represents an added inert buffer gas molecule) can all be prescribed. This assumption with regard to  $Cl_2$  implies the possibility of adding additional chlorine, in excess of  $TlCl$  stoichiometry. Hence, equating production and loss rates for  $TlCl$

$$N_p[\sigma_1 + \sigma_2][TlCl] = v \sigma_5[Tl_o][Cl_2] + k_{10}[Tl_o][Cl][N] \\ + d_1[Tl_o] + p_1 d_m[Tl_m]$$

gives

$$[Tl_o] = \frac{N_p[\sigma_1 + \sigma_2][TlCl] - p_1 d_m[Tl_m]}{d_1 + v \sigma_5[Cl_2] + k_{10}[Cl][N]} \quad (2.19)$$

Balancing the rates for  $\text{Cl}_2$ :

$$k_6[\text{Cl}]^2[\text{N}] = v \sigma_5[\text{Tl}_o][\text{Cl}_2]$$

gives

$$[\text{Cl}] = \left\{ \frac{v \sigma_5[\text{Tl}_o][\text{Cl}_2]}{k_6[\text{N}]} \right\}^{1/2} \quad (2.20)$$

Balancing the rates for  $\text{Tl}_m$

$$N_p \sigma_1[\text{TlCl}] = \left\{ d_m + v \left( \sigma_3[\text{TlCl}] + \sigma_4[\text{Cl}_2] + \sigma_7[\text{Tl}_o] + \sigma_8[\text{M}] + \sigma_9[\text{Cl}] \right) \right\} [\text{Tl}_m]$$

gives

$$[\text{Tl}_m] = \frac{N_p \sigma_1[\text{TlCl}]}{d_m + v \left( \sigma_3[\text{TlCl}] + \sigma_4[\text{Cl}_2] + \sigma_7[\text{Tl}_o] + \sigma_8[\text{M}] + \sigma_9[\text{Cl}] \right)} \quad (2.21)$$

For completeness we may also solve for  $d_2$ , the diffusion loss frequency of  $\text{Cl}$ , by equating production and loss of  $\text{Cl}$ :

$$\begin{aligned} N_p(\sigma_1 + \sigma_2)[\text{TlCl}] + v \sigma_5[\text{Tl}_o][\text{Cl}_2] \\ = d_2[\text{Cl}] + 2k_6[\text{Cl}]^2[\text{N}] + k_{10}[\text{Cl}][\text{Tl}_o][\text{N}] \end{aligned}$$

giving

$$d_2 = \frac{N_p(\sigma_1 + \sigma_2)[TlCl] + v\sigma_5[Tl_o][Cl_2] - 2k_6[Cl]^2[N] - k_{10}[Cl][Tl_o][N]}{[Cl]} \quad (2.22)$$

We can now proceed to calculate all the steady state densities as follows:

1. Prescribe molecular densities  $[TlCl]$ ,  $[Cl_2]$  and  $[M]$ , all the relevant reaction rate parameters,  $p_m$  and  $p_1$ , and the container dimensions.
2. Compute  $d_1$  using Eqs. (2.13), (2.15) through (2.18) and  $N = [M + TlCl + Cl]$ .
3. Compute  $[Tl_o]$  from Eq. (2.19).
4. Compute  $[Cl]$  from Eq. (2.20).
5. Compute  $d_m$  using Eq. (2.13), Eq. (2.15) through (2.18) and  $N = [M + TlCl + Cl]$ .
6. Compute  $[Tl_m]$  from Eq. (2.21).
7. Repeat steps 2 to 6 to solve iteratively for  $[Cl]$ ,  $[Tl_o]$ , and  $[Tl_m]$ .
8. Compute  $p_2$  by
  - a. computing  $d_2$  from Eq. (2.22), then
  - b. computing  $1/\lambda_2^2$  from Eq. (2.13), then
  - c. computing  $\lambda_2$  from Eq. (2.15), then
  - d. computing  $p_2$  from Eq. (2.18).

Step 7 is an iteration loop which allows  $Cl$  and  $Tl_o$  to be included as constituents of the total neutral density  $N$ , which in general is taken to be  $[M] + [TlCl] + [Tl_o] + [Cl_2] + [Cl]$ . For the first iteration  $[Cl] + [Tl_o] + [Cl_2]$  is set to zero.

## 2.2 INPUT DATA

### 2.2.1 Absorption Cross Sections

The total absorption cross for TlCl has been measured as a function of wavelength by Davidovits and Bellisio (1969). We have assumed that the process peaking at a wavelength of 251 nm with a value of  $5 \times 10^{-17} \text{ cm}^2$  is entirely dissociative. The branching of this process has been measured by Van Veen et al. (1981) at 248 nm, giving 71% into the metastable channel. Based on these numbers we assign the following values:

$$\sigma_1 = 3.5 \times 10^{-17} \text{ cm}^2$$

$$\sigma_2 = 1.5 \times 10^{-17} \text{ cm}^2$$

We note however that, in a paper published after completion of the present calculations, Scott and Piper (1986) have reported evidence that only 11% of the absorption at 249 nm leads to atomic fragments. They draw similar conclusions regarding TlBr and TlI, some of which appear to be irreconcilable with the fluorescence quantum efficiency measurements of Maya (1978). If, according to Scott and Piper (1986), the values of  $\sigma_1$  and  $\sigma_2$  are an order of magnitude smaller than indicated above, the present conclusions would need to be modified, primarily regarding the required pump power. The differences are apparent from the sensitivity study described in Section 2.3.5 where, among other things, the effect of decreasing these cross sections by an order of magnitude is explored. Since we are concerned here only with optically thin situations the total absorption cross section is not of direct significance.

### 2.2.2 Quenching Cross Sections

Quenching of  $Tl_m(6^2P_{3/2})$  by a number of gases has been measured by Bellisio and Davidovits (1970). Their value for  $TlCl$  is  $3.9 \times 10^{-15} \text{ cm}^2$ . Liu (1985) obtained results consistent with this value, or possibly larger. In order to treat this important reaction conservatively we assume a value of  $\sigma_3 = 1 \times 10^{-14} \text{ cm}^2$  for most of our calculations, and in addition identify optimized conditions when  $\sigma_3 = 4 \times 10^{-15} \text{ cm}^2$ .

We are not aware of any published data for reaction (2.4). Gedeon et al. (1971) have measured a value of  $1.59 \times 10^{-14} \text{ cm}^2$  for the analogous reaction  $Tl_m(6^2P_{3/2}) + I_2 \rightarrow Tl_o + I_2$ . We therefore assume a value of  $\sigma_4 = 1.5 \times 10^{-14} \text{ cm}^2$ .

The self-quenching cross section, reaction (2.7), has a surprisingly large cross section considering the large energy defect (0.97 eV). A value of  $5.4 \times 10^{-16} \text{ cm}^2$  published by Pickett and Anderson (1969) is supported by the value of  $4.5 \times 10^{-16} \text{ cm}^2$  published by Aleksandrov et al. (1978). We therefore use a value of  $\sigma_7 = 5 \times 10^{-16} \text{ cm}^2$ .

Aleksandrov et al. (1978) have also measured quenching cross sections for a range of buffer gases. Their values for  $N_2$  and Ar are  $5 \times 10^{-20} \text{ cm}^2$  and  $5 \times 10^{-24} \text{ cm}^2$  respectively. Either gas would probably be satisfactory as the buffer M in the present application. We assume a conservative value of  $\sigma_8 = 1 \times 10^{-19} \text{ cm}^2$ .

In the absence of any data on reaction (2.9) we have assumed a value of  $\sigma_9 = 1 \times 10^{-17} \text{ cm}^2$  which is probably conservative based on values for other atomic quenchers.

### 2.2.3 Reformation Reactions

We are not aware of data for reaction (2.5). The analogous reaction  $Tl_o + I_2 \rightarrow TlI + I$  has been measured by Gedeon et al. (1971) to have a cross section of  $1.05 \times 10^{-14} \text{ cm}^2$ .

Three body atomic recombination rate coefficients typically lie in the range  $10^{-31}$  to  $10^{-33} \text{ cm}^6/\text{sec}$ . We assume a common value for

reactions 6a and 6b of  $k_6 = 1 \times 10^{-32} \text{ cm}^6/\text{sec}$  and similarly we assume  $k_{10} = 1 \times 10^{-32} \text{ cm}^6/\text{sec}$ .

#### 2.2.4 Diffusion

Diffusion of  $\text{Ti}_m$  through a number of buffer gases has been measured by Aleksandrov et al. (1978) at 390°C. The values of  $D_o$  in  $\text{N}_2$  and Ar are  $0.47 \text{ cm}^2/\text{sec}$  and  $0.3 \text{ cm}^2/\text{sec}$ , respectively. For our purposes we take the mean of these two values and convert it to the value  $(DN) = 4.4 \times 10^{18} \text{ cm}^{-1} \text{ sec}^{-1}$ . In the absence of other data we use this same value for  $\text{Ti}_o$  and Cl diffusion.

In order to evaluate various reaction rates from the above cross sections we must assign a thermal velocity  $v$ . The assumption of a temperature of ~700K is consistent with the results of the next section. At this temperature the species involved in reaction (2.3) through (2.9) have velocities ranging from  $2.5 \times 10^4 \text{ cm/sec}$  to  $6.5 \times 10^4 \text{ cm/sec}$ . For simplicity we assign a common value of  $v = 4 \times 10^4 \text{ cm/sec}$  to all the relevant species.

In computing the diffusion loss of  $\text{Ti}_m$  and  $\text{Ti}_o$  we assume that all metastable are quenched at the wall (i.e.  $p_m = 1$ ), while  $\text{Ti}_o$  is taken to have various values of its sticking probability in order to explore the relative importance of wall reactions in determining the steady state density of  $\text{Ti}_o$ .

In the calculations presented in the next section the sensitivity of the results to all the assumed input parameters is examined, with the exception of  $p_m$  and  $v$  which are fixed at the values indicated above.

### 2.3 CALCULATIONS

The general procedure used to solve for various sets of self-consistent steady state conditions was derived in Section 2.1. All of the calculations reported here refer to a right-circular cylinder having height  $h_o = 20 \text{ cm}$ , and radius  $r_o = 10 \text{ cm}$ . This is believed to be closed to an optimum size for a single "module," possibly forming part of a larger system in a practical device.

The required concentration of  $Tl_m$  is specified by the need to have a reasonably high absorption probability for an incoming 535 nm photon.

With a physical depth of 20 cm, and an absorption cross section of  $4 \times 10^{-12} \text{ cm}^2$  (C. H. Corliss et al. 1962), an optical depth of unity is achieved with  $[Tl_m] = 1.25 \times 10^{10} \text{ cm}^{-3}$ . In performing various exploratory calculations we have therefore focussed attention on those combinations of input parameters which give values of  $[Tl_m]$  in the region of  $1 \times 10^{10} \text{ cm}^{-3}$ . Four distinct situations have been considered: (1) Only  $TlCl$  and its products are present. (2)  $TlCl$  and its products are present with an inert buffer gas. (3) Excess  $Cl_2$  is added to the  $TlCl$ . (4) Both a buffer gas  $M$ , and excess  $Cl_2$  are added to the mixture. In all cases the temperature is assumed to be sufficiently high for all species to be maintained in the gas phase. This implies a lower limit on the temperature, determined either by the prescribed density of  $TlCl$ , or by the density of  $Tl_o$ . The saturated density of  $Tl_o$  varies from  $10^{11}$  to  $10^{12} \text{ cm}^{-3}$  for  $400^\circ\text{C} < T < 450^\circ\text{C}$ . We therefore regard  $[Tl_o] > 10^{12} \text{ cm}^{-3}$  as undesirably high and have sought conditions giving values closer to  $10^{11} \text{ cm}^{-3}$ .

Exploratory calculations determined that a pumping photon flux density of  $1.28 \times 10^{17} \text{ photons/cm}^2/\text{sec}$ , corresponding to 100 milliwatts/cm<sup>2</sup> of line radiation at 254 nm, was sufficient to sustain a density of  $[Tl_m] \approx 1 \times 10^{10} \text{ cm}^{-3}$  under appropriate conditions. This value of  $N_p$  was employed for essentially all the calculations presented below. The sticking, or rather quenching probability for  $Tl_m$  striking the container walls has been assumed throughout to be unity. The value of  $p_1$ , the sticking probability of  $Tl_o$  was varied over a wide range to explore the relative potential importance of wall reconstitution of  $TlCl$ . In all cases the corresponding sticking probability of  $Cl$ ,  $p_2$ , is left as a free parameter and computed as output, as explained in Section 2.1.

### 2.3.1 No Buffer Gas ( $[M] = 0$ )

In this situation it is appropriate to regard the density of TlCl as the independent variable, and the computed self consistent stoichiometric densities are plotted vs. [TlCl] in Figure 2.3 for the cases  $p_1 = 1$  and 0.1. Stoichiometry is imposed on the solutions by adjusting the input value of  $Cl_2$  so as to achieve equal values of  $\{[Tl_o] + [Tl_m]\}$  and  $\{[Cl] + 2[Cl_2]\}$ . The importance of reaction 2.3 is demonstrated by the two curves for  $[Tl_m]$  corresponding to the indicated values of  $\sigma_3$ , the cross section for quenching of  $Tl_m$  by TlCl. This process is dominant at high [TlCl] densities, causing the density of  $Tl_m$  to saturate at a value where it is quenched by TlCl as rapidly as it is produced from it, i.e.  $[Tl_m] \approx N_p \sigma_1 / v \sigma_3$ .

At sufficiently low densities of TlCl ( $\leq 10^{13}$ ) the dominant loss of  $Tl_m$  is by kinetic free fall to the container walls, where it is quenched. Under these conditions the loss frequency depends only on the container size, and on the wall quenching probability  $p_m$ , set equal to unity for all present calculations. Hence  $[Tl_m]$  increases essential linearly with [TlCl], due to the linearly increasing rate of production. As expected, there is no dependence of  $[Tl_m]$  on the  $Tl_o$  sticking probability  $p_1$ . The  $[Tl_m]$  curves shown apply for both  $p_1 = 1$  and  $p_1 = 0.1$ .

Under the conditions of Figure 2.3,  $Tl_o$  is lost predominantly by wall reconstitution, forming TlCl. At low values of [TlCl], where "free fall" diffusion is occurring, this rate is strongly sensitive to the value of  $p_1$ . The resulting steady state density of  $Tl_o$  varies approximately as  $(2-p_1)/p_1$ , the relevant factor appearing in Eq. (2.16). The transition from "free fall" diffusion to standard diffusion occurs in the region where  $1_o \lambda_i \approx A_o^{-2}$ , as indicated by Eq. (2.15). For the present container this occurs when  $N \approx [TlCl] \approx 6 \times 10^{13} \text{ cm}^{-3}$ , when  $p_1 = 1$ , and at an appropriately higher density when  $p_1 = 0.1$ . This transition causes the dependence of  $[Tl_o]$  on [TlCl] to change from linear to quadratic. The latter dependence arises because the diffusion loss rate of  $Tl_o$  is then decreasing inversely as  $N \approx [TlCl]$ , while its production rate is increasing linearly with [TlCl].

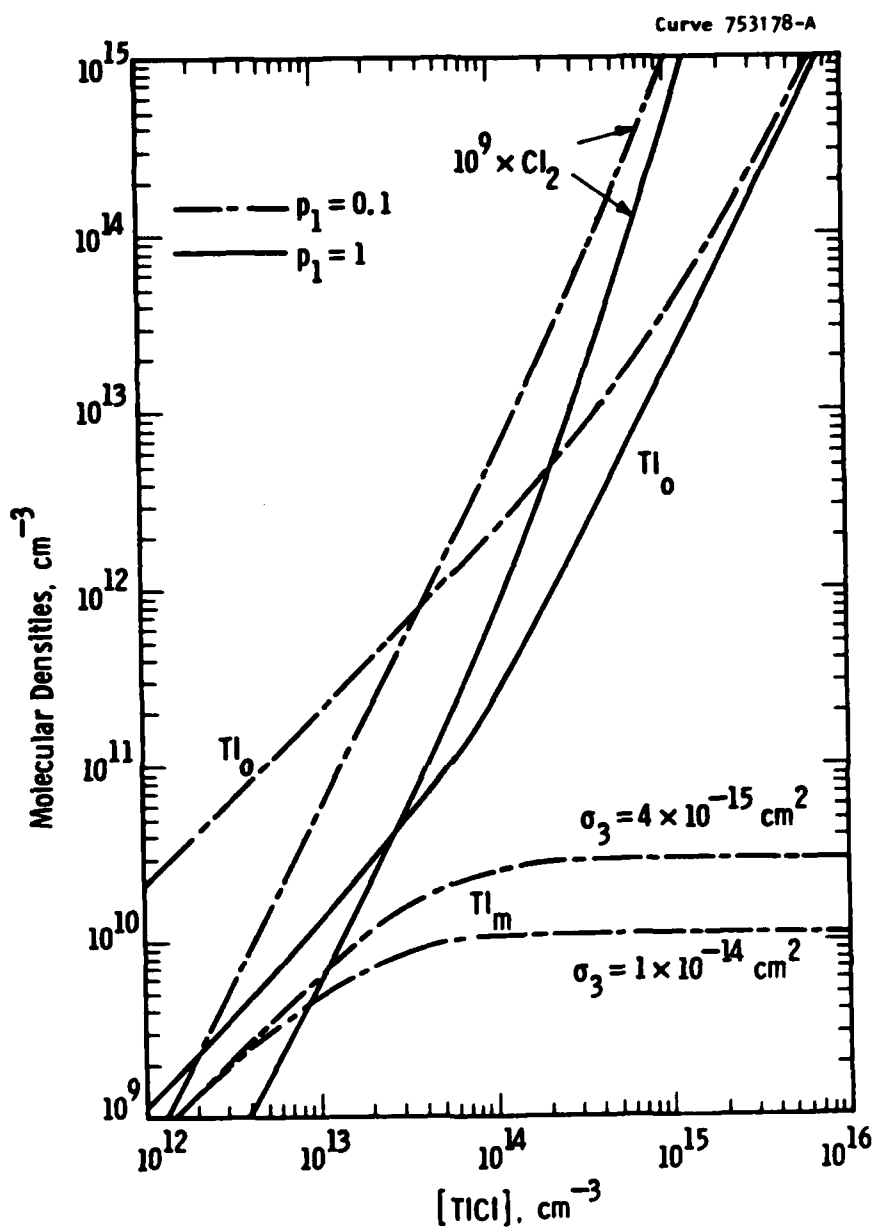


Figure 2.3 Dependence of the important species densities on the density of  $TlCl$ , for a fixed photon flux of  $1.28 \times 10^{17}$  photons/ $\text{cm}^2/\text{s}$ , with no added buffer gas, and with the  $Cl_2$  density adjusted to give stoichiometry. Curves for two values of the sticking probability of  $Tl_0$  are shown, as is the effect on  $Tl_m$  of varying the cross section for reaction 2.3.

The density of Cl is not shown explicitly in Figure 2.3. Over most of the range it is essentially the same as  $[Tl_o]$ , since stoichiometry requires  $[Tl_o] + [Tl_m] = [Cl] + 2[Cl_2]$ , and  $[Cl_2]$  is extremely small.

Of particular interest is the  $Tl_o$  density when  $[Tl_m]$  approaches saturation. This depends on the  $Tl_o$  sticking probability. For  $p_1 = 1$  the relevant  $Tl_o$  density is  $< 10^{11} \text{ cm}^{-3}$ , and with  $p_1 = 0.1$  the value rises to  $\sim 10^{12} \text{ cm}^{-3}$ . The latter may imply undesirably high temperature, and we therefore seek a method other than wall recombination for reducing the equilibrium density of  $Tl_o$ . The possibility of accelerating the three-body volume recombination processes by adding an otherwise inert buffer gas is explored in the next subsection.

### 2.3.2 With Buffer Gas, "M"

The effect of adding a buffer gas to the mixture has been investigated with a view to enhancing the three-body volume recombination processes by which atomic thallium and chlorine are reconstituted to  $TlCl$ . As an example we show in Figure 2.4 the effects on the situation when a value of  $p_1 = 0.1$  is assumed. The chain curves, for no buffer gas, are reproduced from Figure 2.3. The addition of a buffer gas density of  $3 \times 10^{18} \text{ cm}^{-3}$  gives the situation represented by the full curves. As expected, the density of  $Tl_m$  approaches saturation at a much lower density of  $TlCl$  due to the suppression of the free fall diffusion loss. Similarly, the densities of  $Tl_o$  and Cl increase together in the presence of the buffer gas, due to inhibition of their transport to the wall where their recombination is primarily occurring. There is no evidence that the volume recombination processes have been made effective by this amount of added buffer gas, and the overall effect is that, in the region where  $[Tl_m]$  is close to its saturated level, the density of  $Tl_o$  has increased over the corresponding value without the buffer gas. Increasing the buffer gas density too much

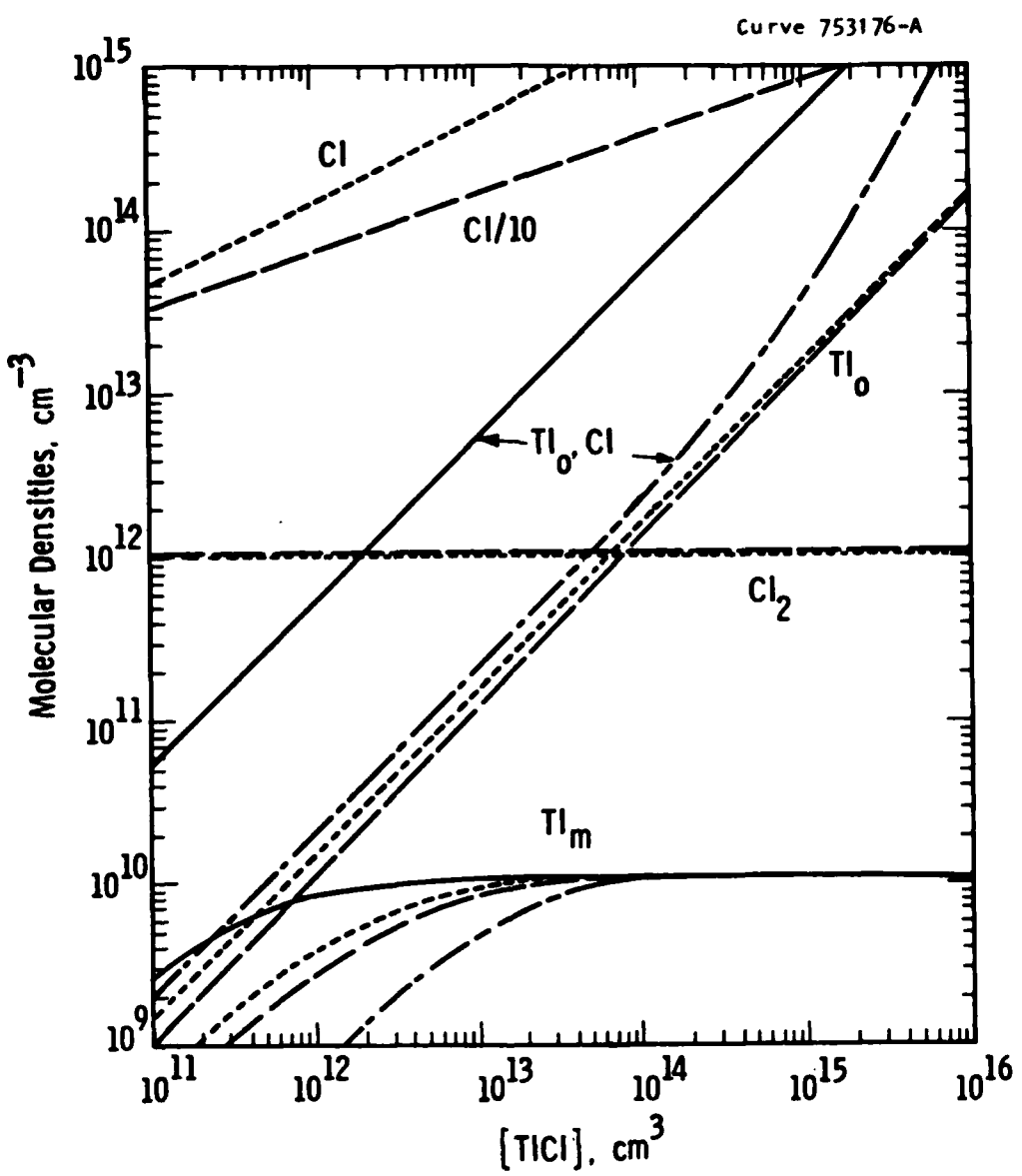


Figure 2.4 Showing the effects of adding a buffer gas and/or  $\text{Cl}_2$ , with the  $\text{Tl}_0$  sticking probability of 0.1. The dot-dash curves, taken from Figure 2.3, correspond to no buffer gas and stoichiometry. The effect of adding  $\text{Cl}_2$  to maintain its density at  $1 \times 10^{12} \text{ cm}^{-3}$  is shown by the long-dash curves, and the effect of also adding  $3 \times 10^{16} \text{ cm}^{-3}$  of buffer gas is shown by the short dash curve. The full curves correspond to a buffer gas density of  $3 \times 10^{16} \text{ cm}^{-3}$  with the  $\text{Cl}_2$  density adjusted for stoichiometry.

higher levels is a viable option if pressure broadening of the absorption line is needed. However, the use of substantially higher buffer gas densities can cause noticeable reduction of the  $Tl_m$  density, due to collisional quenching. This effect is seen in Figure 2.5, where the various densities are plotted as a function of the buffer gas density for a constant  $TlCl$  density of  $1 \times 10^{13} \text{ cm}^{-3}$ . In this figure the broken curves represent the situation presently being considered, where only  $TlCl$  and its stoichiometric products are present with the buffer gas. The peak in the density of  $Tl_o$  occurs in the region of  $[M] = 6 \times 10^{17} \text{ cm}^{-3}$ , where the volume recombination processes start to control the densities of  $Tl_o$  and  $Cl$ . At low buffer gas densities  $[Tl_o]$  is sensitive to its sticking probability,  $p_1$ , whose value is indicated on some of the curves in Figure 2.5. Where not indicated, the curves are insensitive to this parameter. It is clear from this figure that the only advantage of adding a buffer gas to an otherwise stoichiometric mixture derived from  $TlCl$  is a modest increase in the sustained density of metastables, this being achieved at the expense of a significant increase in the ground state metal atom density,  $[Tl_o]$ .

### 2.3.3 With Extra Chlorine

As an alternative technique for controlling the density of atomic thallium we consider now the use of excess chlorine. To investigate this possibility a series of calculations were performed in which the density of  $Cl_2$  was prescribed at some fixed value, without concern for the overall stoichiometry. The effect of adding a  $Cl_2$  density of  $1 \times 10^{12} \text{ cm}^{-3}$  is represented in Figure 2.4 by the long-dashed curves, which should be compared to the dot-dash curves representing the situation with no additives. Note that  $[Tl_o]$  has decreased over the whole range of  $TlCl$  densities, while  $[Tl_m]$  has increased at low densities. As a result, in the region where  $[Tl_m]$  now approaches saturation, there is a substantial decrease in the  $Tl_o$  density to a value of approximately  $1 \times 10^{11} \text{ cm}^{-3}$ .

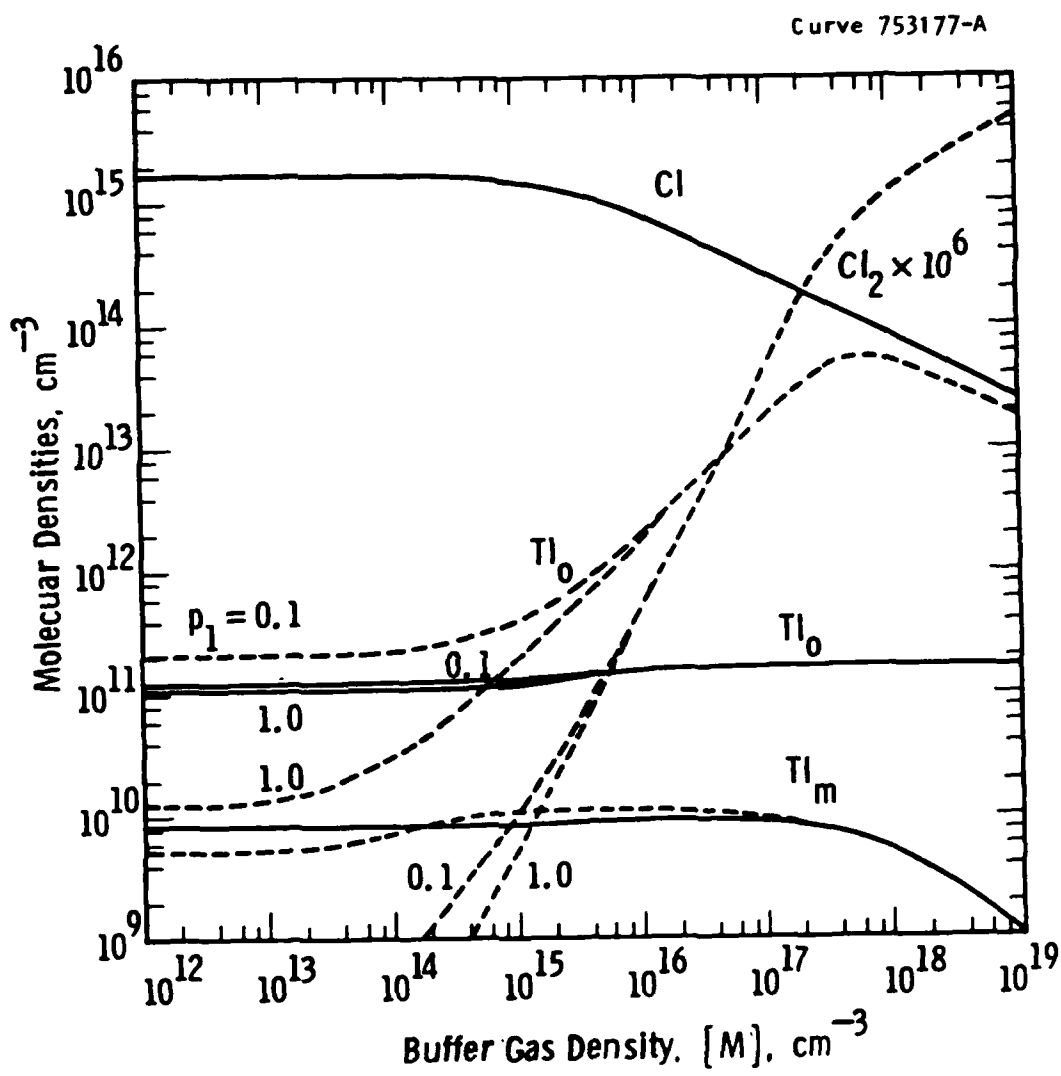


Figure 2.5 Showing the dependence on buffer gas density, for a fixed  $TlCl$  density of  $1 \times 10^{13} \text{ cm}^{-3}$ . The broken curves correspond to stoichiometry for  $Cl_2$ , while the full curves are for a fixed  $Cl_2$  density of  $1 \times 10^{12} \text{ cm}^{-3}$ . Curves for two values of the  $Tl_0$  sticking probability are shown where there is a sensitivity to this parameter.

The effect of varying the density of  $\text{Cl}_2$  over a wide range is illustrated in Figure 2.6 for a constant  $\text{TiCl}$  density of  $1 \times 10^{13} \text{ cm}^{-3}$ , and assuming a sticking probability of  $p_1 = 0.03$  for  $\text{Ti}_o$  at the wall. The broken curves represent the situation presently being considered, where only  $\text{Cl}_2$  is added to the  $\text{TiCl}$ . We note that densities of  $\text{Cl}_2$  greater than  $1 \times 10^{10} \text{ cm}^{-3}$  are effective in reducing the density of  $\text{Ti}_o$ , while the  $\text{Ti}_m$  density is essentially unaffected until the  $\text{Cl}_2$  density exceeded  $1 \times 10^{12} \text{ cm}^{-3}$ . Thus it is clear that the addition of modest amounts of excess  $\text{Cl}_2$  provides control of the steady state density of  $\text{Ti}_o$ .

#### 2.3.4 With Added Chlorine and Buffer Gas

A number of calculations were performed to explore the possible advantages of adding both a buffer gas and excess chlorine. In Figure 2.4 the short dashed curves represent the situation where  $[\text{M}] = 3 \times 10^{16} \text{ cm}^{-3}$  and  $[\text{Cl}_2] = 1 \times 10^{12} \text{ cm}^{-3}$ . Compared to the long dashed curves representing the case with only  $\text{Cl}_2$  added, these show a minor increase in the sustained density of  $\text{Ti}_m$  accompanied by a similar increase in  $[\text{Ti}_o]$ . The effect of varying the buffer gas density over a wide range, while maintaining  $[\text{Cl}_2] = 1 \times 10^{12} \text{ cm}^{-3}$  is shown by the full curves in Figure 2.5. The main effect of the excess chlorine is that its controls the density of  $\text{Ti}_o$  over the whole range, with only a slight dependence of  $[\text{Ti}_o]$  on the sticking probability  $p_1$  at the lower buffer gas densities. In this region of  $[\text{M}]$  we note that the effect of the excess chlorine on  $[\text{Ti}_o]$  depends significantly on the magnitude of  $p_1$ . When this parameter is small, addition of  $\text{Cl}_2$  causes  $[\text{Ti}_o]$  to decrease, due to the effect of reaction (2.5). On the other hand, if  $p_1$  is close to unity, the high atomic chlorine density arising from the added chlorine inhibits the transport of  $\text{Ti}_o$  to the wall, causing its volumetric concentration to increase.

The effects of varying the chlorine density with a fixed buffer gas density of  $3 \times 10^{16} \text{ cm}^{-3}$  is shown by the full curves in Figure 2.6, where a small value of  $p_1 = 0.03$  has been assumed. In the region of

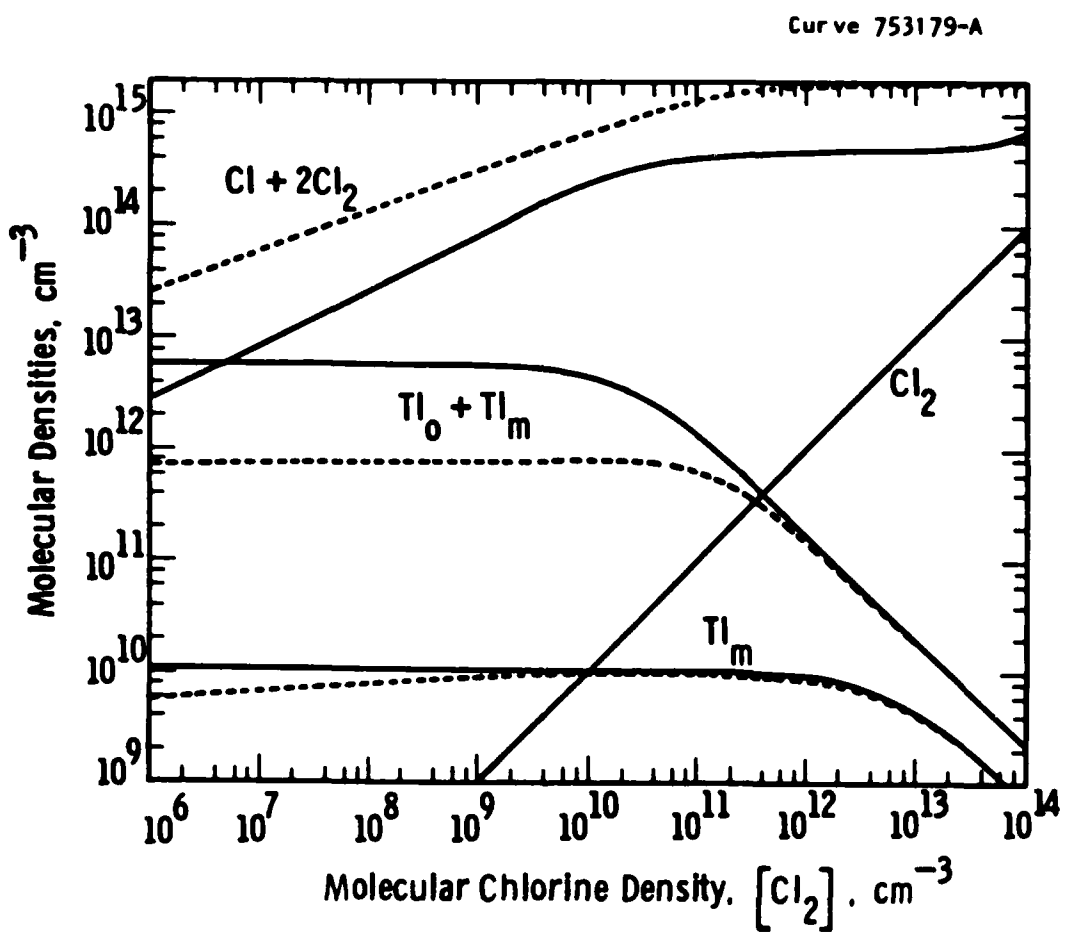


Figure 2.6 Showing the effect of varying the density of  $\text{Cl}_2$  over a wide range, for a constant  $\text{TlCl}$  density of  $1 \times 10^{13} \text{ cm}^{-3}$ , and a constant  $\text{Tl}_0$  sticking probability of 0.03. The broken curves correspond to no added buffer gas, while the full curves are for a fixed buffer gas density of  $3 \times 10^{16} \text{ cm}^{-3}$ .

$[Cl_2] \approx 1 \times 10^{12} \text{ cm}^{-3}$ , where the  $Tl_o$  density has been reduced substantially without significantly affecting the metastable density, we see that additional buffer gas has very little influence on either  $Tl_o$  or  $Tl_m$ .

### 2.3.5 Sensitivity Study

In the preceding subsections we have explored the effects of varying the physically controllable densities, of  $TlCl$ ,  $Cl_2$ , and buffer gas  $M$ . In addition the cross section for reaction (2.3), and the  $Tl_o$  sticking probability  $p_1$  have been varied. It appears from these results that there exists a rather extensive parameter space within which it is possible to sustain the desired density of metastables with modest optical pumping power levels. It is important to establish that this conclusion does not rest on some fortuitous circumstance dependent on the assumptions made regarding the many other parameters involved in the model. To this end, additional calculations have been performed where, in turn, each input parameter was first increased a factor of ten, and then decreased a factor of ten from its baseline value. The chosen baseline case parameters follow from the considerations discussed in Section 3, or from the results presented above.

The results of this sensitivity study are presented in Table 2.2. The parameters involved are listed in the first column, followed in the second column by the values assigned. The final three columns give the atomic densities of interest. The first row corresponds to our baseline case around which the variations are being explored. For this case each parameter listed has a value equal to the geometric mean of the two values listed in the table. For example, for this case,  $\sigma_1 = 3.5 \times 10^{16} \text{ cm}^2$ , as indicated in the first row, while  $\sigma_2 = 1.5 \times 10^{-17} \text{ cm}^2$  etc.

Examination of this table reveals certain anticipated sensitivities. The sustained density of metastables is more or less proportional to the parameters  $\sigma_1$  and  $N_p$ , which control the rate of reaction (2.1). Reaction (2.2) plays a significant role in determining

the density of  $Tl_o$ , but has essentially no effect on the metastable density. The converse is true of reaction (2.3), whose effect was explored somewhat in Figure 2.3. Reaction (2.4) is quenching of metastables by  $Cl_2$ , and the effects of varying  $\sigma_4$  are consistent with the effect of varying  $[Cl_2]$  illustrated in Figure 2.6. Reaction (2.5) plays a dominant role in controlling the density of  $Tl_o$ , whose density is seen to be essentially inversely proportional to  $\sigma_5$ . The only other significant sensitivity is to the pumping photon flux density,  $N_p$ . Changes in the magnitude of this parameter cause changes in the densities of  $Tl_o$  and  $Tl_m$  which are similar to the effects of the changes made in  $\sigma_2$  and  $\sigma_1$  respectively. Since  $N_p$  is subject to external control it can in principle be adjusted to compensate for any error in the assumed value of  $\sigma_1$ .

Table 2.2

<u>Input Parameter</u>	<u>Value</u>	<u>[Tl<sub>o</sub>]</u>	<u>[Cl]</u>	<u>[Tl<sub>m</sub>]</u>
		<u>cm<sup>-3</sup></u> <u>1E+11</u>	<u>cm<sup>-3</sup></u> <u>1E+15</u>	<u>cm<sup>-3</sup></u> <u>1E+09</u>
$\sigma_1 \text{ cm}^2$	3.5E-17	1.58	0.46	9.25
	3.5E-18	0.58	0.28	0.94
	3.5E-16	11.53	1.22	86.82
$\sigma_2 \text{ cm}^2$	1.5E-18	1.15	0.39	9.30
	1.5E-16	5.84	0.87	8.94
$\sigma_3 \text{ cm}^2$	1.0E-15	1.58	0.46	34.54
	1.0E-13	1.58	0.46	1.11
$\sigma_4 \text{ cm}^2$	1.5E-15	1.58	0.46	10.39
	1.5E-13	1.58	0.46	4.41
$\sigma_5 \text{ cm}^2$	1.0E-15	12.59	0.41	9.25
	1.0E-13	0.16	0.46	9.25
$k_6 \text{ cm}^6/\text{s}$	1.0E-33	1.58	1.42	8.58
	1.0E-31	1.58	0.14	9.49
$\sigma_7$	5.0E-17	1.58	0.46	9.26
	5.0E-15	1.58	0.46	9.20
$\sigma_8$	1.0E-20	1.58	0.46	9.46
	1.0E-18	1.58	0.46	7.59
$\sigma_9$	1.0E-18	1.58	0.46	9.57
	1.0E-16	1.58	0.46	6.94
$k_{10} \text{ cm}^6/\text{s}$	1.0E-33	1.58	0.46	9.25
	1.0E-31	1.57	0.45	9.25
ND/cm.s.	2.2E+18	1.60	0.46	9.26
	8.8E+18	1.54	0.45	9.24
$p_1$	1.0E+00	1.58	0.46	9.25
	1.0E-02	1.59	0.46	9.25
$N_p \text{ ph/cm}^2\text{s}$	1.3E+16	0.16	0.14	0.95
	1.3E+18	15.79	1.42	85.36

### 3. THE Tl-Cs SYSTEM

#### 3 COLLISIONAL TRANSFER EXCITATION

The collisional transfer excitation of the metastable state of thallium atoms involves introducing into thallium vapor another species with resonance states in the vicinity of the metastable state level of Tl, to which the collisional transfer from those resonance states can easily take place. Figure 3.1 shows a partial energy level diagram which includes the thallium states involved as well as some appropriate cesium states. The radiation-trapped Cs( $6^2P$ ) states have long lifetimes and then can transfer energy to ground state Tl atoms to excite them to the metastable state Tl( $2^2P_{3/2}$ ) through collisions. The transfer excitation rate is a strong function of the energy defect between the two states involved (Czajkowski et al., 1973), in this case about 0.4 eV. The excitation transfer cross sections are estimated to be  $2 \times 10^{-17} \text{ cm}^2$  for the Tl-Cs system.

Table 3.1 lists the various reactions and their cross sections relevant to the performance of an ALF employing Cs-Tl mixtures. Those cross sections not available in the literature have been estimated. The sustained density of Tl<sub>m</sub> depends primarily on the balance between production by Reaction (3.2) and loss by reactions (3.5) and (3.6). The corresponding density of Cs<sup>\*</sup>( $6P$ ) that needs to be sustained is thus given by

$$[\text{Cs}^*(6P)] = \text{Tl}_m \left\{ \frac{\left[ \frac{\text{Cs}_0}{\text{Tl}_0} \right] \sigma_5}{\left[ \frac{\text{Tl}_0}{\text{Cs}_0} \right] \sigma_2} + \frac{\sigma_6}{\sigma_2} \right\} \quad (3.0)$$

The pumping power required to sustain this density is determined primarily by Reaction 8 and the radiative loss of Cs<sup>\*</sup>( $6P$ ) modified by

Curve 745873-A

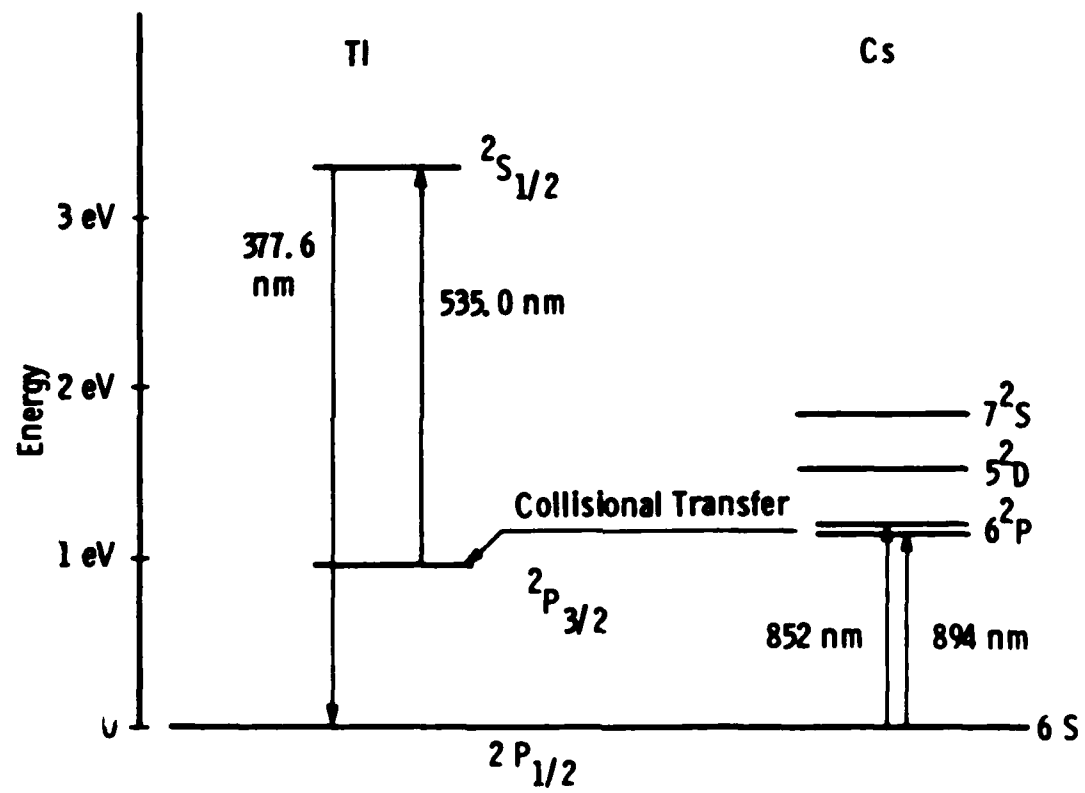


Figure 3.1 Partial energy level diagram of Tl and Cs.

Table 3.1  
List of Reactions and Cross Sections

<u>Reactions</u>	<u>Cross Sections (cm<sup>2</sup>)</u>
(1) $\text{Cs}(6S) + h\nu(890) \xrightarrow{\sigma_1} \text{Cs}^*(6P)$	$\sigma_1 = 1.7 \times 10^{-11}$
(2) $\text{Cs}^*(6P) + \text{Tl}(^2P_{1/2}) \xrightarrow{\sigma_2} \text{Tl}^m(^2P_{3/2}) + \text{Cs}(6S) + \Delta E$	$\sigma_2 = 2 \times 10^{-17}$
(3) $\text{Tl}^m(^2P_{3/2}) + h\nu(535) \xrightarrow{\sigma_3} \text{Tl}^*(7S)$	$\sigma_3 = 4.9 \times 10^{-12}$
(4) $\text{Tl}^*(7S) \xrightarrow{\sigma_4} \text{Tl}(^2P_{1/2}) + h\nu(378)$	$\sigma_4 = 3 \times 10^{-12}$
(5) $\text{Tl}^m(^2P_{3/2}) + \text{Cs}(6S) \xrightarrow{\sigma_5} \text{Tl}(^2P_{1/2}) + \text{Cs}(6S) + \Delta E$	$\sigma_5 = 5 \times 10^{-18}$
(6) $\text{Tl}^m(^2P_{3/2}) + \text{Tl}(^2P_{1/2}) \xrightarrow{\sigma_6} 2\text{Tl}(^2P_{1/2}) + \Delta E$	$\sigma_6 = 5 \times 10^{-16}$
(7) $\text{Cs}^*(6P) + \text{Tl}(^2P_{1/2}) \xrightarrow{\sigma_7} \text{Cs}(6S) + \text{Tl}(^2P_{1/2}) + \Delta E$	$\sigma_7 = 5 \times 10^{-18}$
(8) $\text{Cs}^*(6P) + \text{Cs}(6S) \xrightarrow{\sigma_8} 2\text{Cs}(6S) + \Delta E$	$\sigma_8 = 2.1 \times 10^{-14}$
(9) $\text{Cs}^*(6P) + \text{Cs}^*(6P) \xrightarrow{\sigma_9} \text{Cs}^{**}(6D) + \text{Cs}(6S) + \Delta E$	$\sigma_9 = 1.5 \times 10^{-15} - 2 \times 10^{-14}$
(10) $\text{Cs}^*(6P) + h\nu(377) \xrightarrow{\sigma_{10}} \text{Cs}^+ + e$	$\sigma_{10} = 10^{-19}$
(11) $\text{Cs}^*(6P) + \text{Tl}^*(7S) \xrightarrow{\sigma_{11}} \text{Cs}^+ + \text{Tl}(^2P_{1/2}) + e$	$\sigma_{11} = 5 \times 10^{-14}$
(12) $\text{Cs}^*(6P) + \text{Cs}^*(6P) \xrightarrow{\sigma_{12}} \text{Cs}_2^+ + e$	$\sigma_{12} = 1.5 \times 10^{-15}$

resonance radiation trapping. Together, these processes impose an effective lifetime of  $\tau_{\text{eff}}$  on the  $\text{Cs}^*(6P)$  atoms. This effect has been studied in pure Cs by recording the growth and decay of the fluorescence signals from both resonance states following the pumping of one or other of the states by a short pulse from a tunable dye laser.

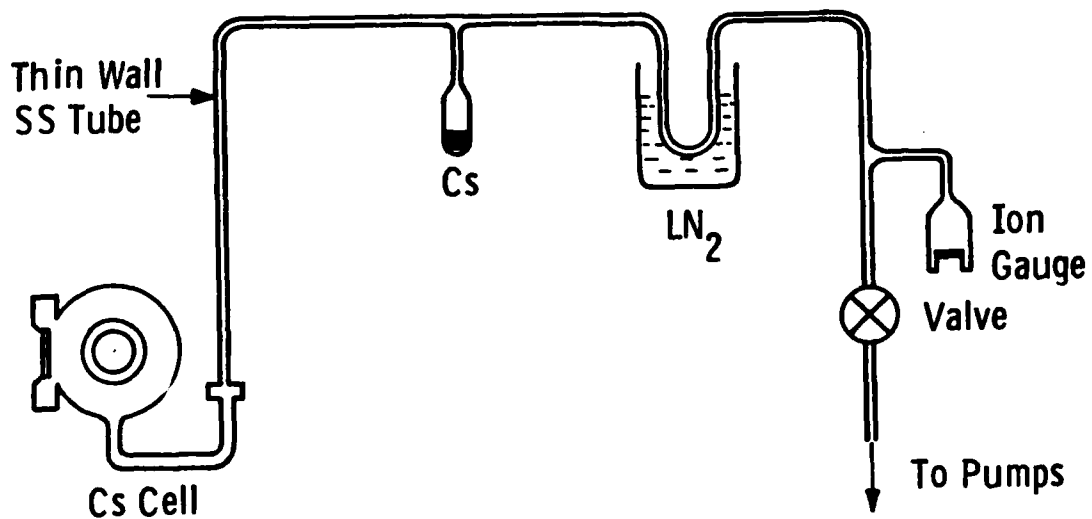
### 3.2 THE EXPERIMENT

A long cylindrical shape was chosen for the experimental cell to approximate the atomic line filter geometry. For the apparent lifetime study of the  $\text{Cs}(6P_{1/2})$  and  $\text{Cs}(6P_{3/2})$  states we have used for the excitation a laser pulse which is short compared to the natural lifetimes. This simplifies the analysis of the measured time dependent fluorescence of the parent state and the excitation transferred state. The cesium vapor density covered in the present experiment ranges from  $10^{11} \text{ cm}^{-3}$ , where the Doppler effect dominates the line shape, to  $10^{14} \text{ cm}^{-3}$ , where collisional effects dominate the line shape. We describe first the physical characteristics and the preparation procedure of the cesium cell, and we then describe the experimental setup and the method by which the data are collected and prepared for analysis.

#### 3.2.1 The Cesium Cell

The cesium cell is a cylinder made of 304 stainless steel, 23 cm long and inside diameter 11.5 cm, simulating one module of the atomic line filter. It is shown schematically in Figures 3.2 and 3.3. It has three optical ports, each made of ~3 mm thick sapphire brazed to a kovar sleeve and mounted on a standard size Varian vacuum flange. The two end ports are ~25 mm in diameter, allowing the excitation laser pulse to pass through the cesium cell. The third port, ~50 mm in diameter, is mounted approximately mid-way on the side wall and is oriented 90° to the first two. An ~2  $\mu\text{m}$  thick layer of nickel is coated electrolytically on the sapphire metal joints to prevent their deterioration from cesium attack. The copper gaskets for sealing the

Dwg. 9387A56



Cs Cell Preparation Scheme

Figure 3.2 The material handling system used to prepare the Cs cell.

sapphire window flange to the cell body are also plated with  $\sim 200$  Å of nickel.

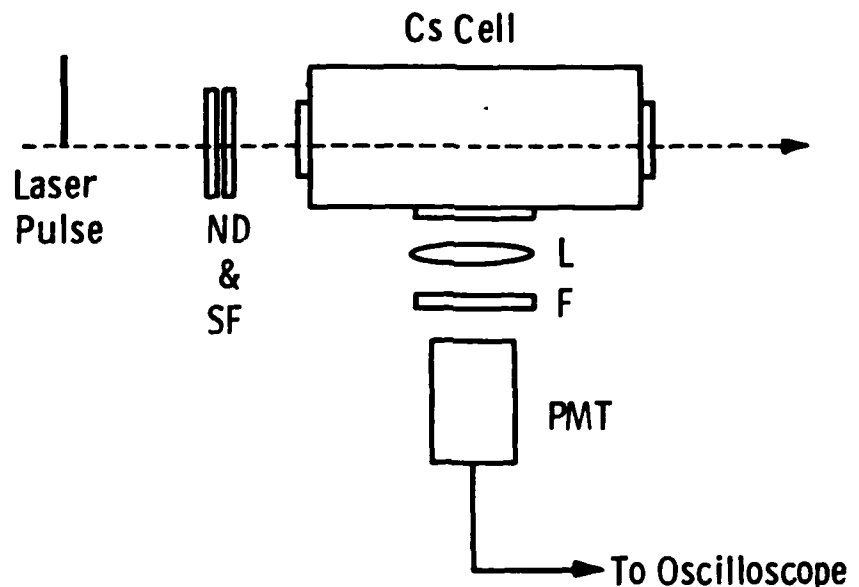
The arrangement used to vacuum process the cell is shown in Figure 3.2. A 13 mm diameter U-tube to be used as the cesium reservoir is welded to the center bottom of the cesium cell. The other end of the U-tube has a 15 cm long straight section of thin wall ( $\sim 0.25$  mm) stainless steel tubing connecting the cesium cell to a conventional high vacuum system. While pumping, the cell is baked at  $\sim 400^\circ\text{C}$  for 12 hours or more until a vacuum of  $\sim 10^{-8}$  torr is attained. Prepurified cesium in a glass capsule is then opened and about 2 grams of it is distilled into the cell. The thin wall stainless steel tubing is pinched to form a sealed bridge, and a controlled amount of current is passed through the bridge to form a resistive weld, thereby capping off and separating the cesium reservoir from the vacuum system. The cesium cell is then transferred to the experimental station described in the next subsection.

### 3.2.2 Experimental Apparatus

The apparatus used to determine the effective lifetimes of the  $\text{Cs}(6\text{P}_{1/2})$  and  $\text{Cs}(6\text{P}_{3/2})$  states is shown schematically in Figure 3.3. There are three major components: (1) the cesium cell which provides the proper container shape and the necessary cesium vapor density, (2) the tunable dye laser that provides pulse excitation of the cesium vapor, and (3) the components for detection and display of the time dependence of the direct and the excitation exchange fluorescence signals.

After processing, the cesium cell is housed in a specially constructed oven made of 8.4 cm thick fire bricks, the inside lining of which is made of 1.5 mm aluminum sheets. Three sets of heaters are used, one set on the ceiling panel, one set on the bottom panel and one set on the side walls. Ten thermocouples strategically attached to the cesium cell body monitor its temperature distribution. Heater powers are adjusted such that the cell body temperature is always higher than

Dwg. 9387A55



L = Lens

SF = Step Filter

F = Narrow Band Filter

ND = Neutral Density Filter

PMT = Photomultiplier

Figure 3.3 The optical arrangement used to pump and view the Cs fluorescence.

that of the cesium reservoir, the difference being a few degrees at low cesium densities, to as high as 30°C at high densities. Once the cell body reaches a predetermined temperature, a temperature controller regulates the power to the heaters. Temperature stability of the cesium cell can normally be maintained to within 1°C.

There are three double-walled quartz windows 5 cm in diameter in the oven's side walls, aligned with the cesium cell's sapphire windows. Two of these windows are for the entrance and exit of the excitation laser pulse, and the third one 90° to the other two is for the observation of the fluorescence.

The cesium vapor is optically pumped by a pulsed and spectrally tunable dye laser (Quanta Ray Model DCR/PDL) pumped by a Nd:YAG laser which is flash-lamp-pumped, Q-switched and frequency doubled to 532 nm for the dye laser pumping. With Exciton LDS 867 dye and at 10 Hz the dye laser output is ~200 nJ per pulse at wavelengths 852 nm or 894 nm. The laser pulse duration is ~9 ns and the spectral width is ~0.4 cm<sup>-1</sup>. The laser beam axis is aligned collinearly with that of the cesium cell. The unstable oscillator resonator design of the Nd:YAG laser results in a donut shaped pump beam. This in turn produces a donut shaped dye laser beam measuring ~6 mm outside diameter and ~3 mm inside diameter. Because the dye fluoresces strongly at the pump frequency (532 nm), a Schott RG 830 red filter is placed at the entrance port of the cesium cell to preclude any possible interference with the time dependent resonance photon transport processes. The dye laser output is usually measured with a Scientech 362 power meter at a point between the RG 830 red filter and the entrance port to the cesium cell, prior to and shortly after each experimental run. When tuned and stabilized properly we find no significant change of laser output at the set wavelength over a period of an hour. The laser excitation pulse energy was reduced by predetermined amounts with a calibrated neutral density filter to check for any dependence of the time dependent resonance fluorescence on power density. For the laser excitation pulse energy used in the present experiment there is no noticeable effect on the measured effective lifetime of either the Cs(6P<sub>1/2</sub>) or the Cs(6P<sub>3/2</sub>) state.

### 3.3 852 nm AND 894 nm FLUORESCENCE FROM PULSE EXCITED Cs(6P<sub>1/2</sub>) AND Cs(6P<sub>3/2</sub>) STATES

#### 3.3.1 Experimental Conditions

After reaching a prescribed cesium vapor density in the cell, the dye laser system was turned on and tuned to either 852 nm or 894 nm wavelength for resonance excitation of the Cs(6P<sub>3/2</sub>) or the Cs(6P<sub>1/2</sub>) state. To avoid initial nonuniform excitation along the axial direction of the long cesium cell we set the dye laser pulse energy at a level exceeding the burn-through or column saturation value. The latter is defined as that power density which provides approximately one resonance photon for each atom in the laser beam column per radiative lifetime [Huennekens and Gallagher 1983]. That is,

$$I_{\text{col.sat.}} = \left[ \frac{NL h\nu_{12}}{\tau_n} \right] \left[ \frac{\Delta\nu_{\text{laser}}}{\Delta\nu_{\text{atom}}} \right] \quad (3.13)$$

where  $N$  is the cesium atom density,  $L$  is the column length,  $h\nu_{12}$  is the resonance photon energy,  $\tau_n$  is the natural lifetime of the upper state [Cs(6P<sub>3/2</sub>) or Cs(6P<sub>1/2</sub>)], and  $\Delta\nu_{\text{laser}}$  and  $\Delta\nu_{\text{atom}}$  are the laser line width and atomic absorption line width, respectively. The ratio  $\Delta\nu_{\text{atom}}/\Delta\nu_{\text{laser}}$  represents the fraction of laser photons that can be absorbed by the atoms and is set equal to 1 if  $\Delta\nu_{\text{atom}} \geq \Delta\nu_{\text{laser}}$ . If the laser pulse duration  $\tau_L$  is shorter than the atomic natural lifetime,  $\tau_n$  should be replaced by  $\tau_L$  in Equation (3.13). For example the absorption equivalent width for 852 nm at  $N = 6 \times 10^{12} \text{ cm}^{-3}$  is approximately 8.2 GHz [see next section] while the laser linewidth is ~12 GHz. The laser pulse duration of 9 nsec is much smaller than the natural lifetime of 30.5 nsec for the Cs(6P<sub>3/2</sub>) state. Therefore

$$I_{\text{column sat}} \approx 2.6 \times 10^3 \text{ Watt/cm}^2$$

This is about a factor a fifty smaller than the laser pulse intensity of  $1.1 \times 10^5$  Watt/cm<sup>2</sup> at 200 mJ per pulse when unattenuated. Therefore for all practical purposes we have a column saturation condition (or burn-through condition), the cesium atoms within the cell are more or less uniformly excited in the axial direction along the laser beam path.

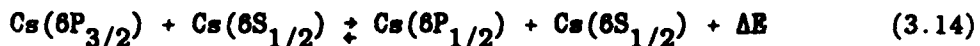
To facilitate the data reduction it is desirable that the spatial distribution of the resonance excitation relax quickly to the fundamental mode [Holstein 1947, 1951]. This mode is strongly excited initially by the on-axis pumping, and higher order modes will in any event decay much more rapidly [van Trigt 1969]. The assumption that only the fundamental mode contributes to the measured decay rates is therefore reasonable, and is consistent with the observed double exponential character of the decays.

### 3.3.2 Data Acquisition

After column saturation pulse excitation of the cesium vapor to the (6P<sub>1/2</sub>/6P<sub>3/2</sub>) state with 894/852 nm laser light pulse, the time dependence of the direct 894/852 nm fluorescence and of the excitation transferred 852/894 nm fluorescence are measured. A 75 mm diameter, 130 mm focal length lens is placed close to the double-walled quartz oven window to collect the fluorescent light from the mid-section of the cell and focus it on the S1 photocathode of the K2276 photomultiplier (PMT). Each line is isolated by a narrowband (~10 nm FWHM) interference filter having a peak transmittance of ~45%. Linearity of the PMT response is checked with a set of calibrated neutral density filters, and is found to be adequate. The electron transit dispersion time of the PMT is reported to be a few nanoseconds which is adequate for the present purposes. Output of the PMT is fed to a Tektronix 7834 storage oscilloscope equipped with a 7A26 dual trace amplifier that is terminated with a 100 Ohm resistor. The bandwidth of the 7A26 amplifier is dc to 200 MHz, when terminated with a 50 Ohm load. The recorded traces are photographed. Subsequently the photographs were enlarged to a size convenient for digitizing using a digitally interfaced plotter (Tektronix Model No. 4662).

Figures 3.4, 3.5 and 3.6 are typical oscilloscope traces of the direct and excitation transfer fluorescence at three different cesium densities:  $2.55 \times 10^{11} \text{ cm}^{-3}$ ,  $7.3 \times 10^{12} \text{ cm}^{-3}$ , and  $2.3 \times 10^{14} \text{ cm}^{-3}$ , respectively. The dye laser pulse width is  $\sim 9 \text{ ns}$  and the laser pulse repetition rate is 10 Hz. Subsequent analysis shows that these three examples represent different regimes. At the lowest cesium density the decay is dominated by radiation trapping of the Doppler broadened lines, at the intermediate density the line is collisionally broadened, while at the highest density collisional self quenching dominates the observed decays.

The energy difference between the  $6P_{3/2}$  and the  $6P_{1/2}$  state is only 0.069 eV. Therefore the following exchange collisions are effective in the temperature range of our experiment,  $318^{\circ}\text{K}$  to  $457^{\circ}\text{K}$ ,



where  $\Delta E$  is the energy defect, and can be taken up by the thermal energy of the participants. Therefore experimentally the intensity of the excitation exchange fluorescence should be a linear function of the direct fluorescent. This is shown in Figure 3.7 where the dye laser wavelength is tuned to the  $6P_{1/2}$  state (894 nm), and the direct (894 nm) and the excitation exchange (852 nm) fluorescence are both measured as a function laser power keeping the cesium vapor density at  $7.3 \times 10^{12} \text{ cm}^{-3}$ .

Figures 3.8 and 3.9 show examples of the late time behavior observed at a density of  $7.3 \times 10^{12} \text{ cm}^{-3}$  following excitation with a laser pulse power of  $\sim 2.2 \times 10^4$  Watts, or  $200 \mu\text{J}$  per pulse at 852 nm and 894 nm respectively. In these cases simple linear fits to the data are indicated. As predicted by the analysis of the next section, all have essentially the same time constant, in this case  $27 \mu\text{s}$ . We have checked for any effects of the laser pulse power on the fluorescent time constants. Figure 3.10 is a plot of the late time fluorescent decays of 894 nm light at 200 mJ/pulse and 63 mJ/pulse excitation levels. Here

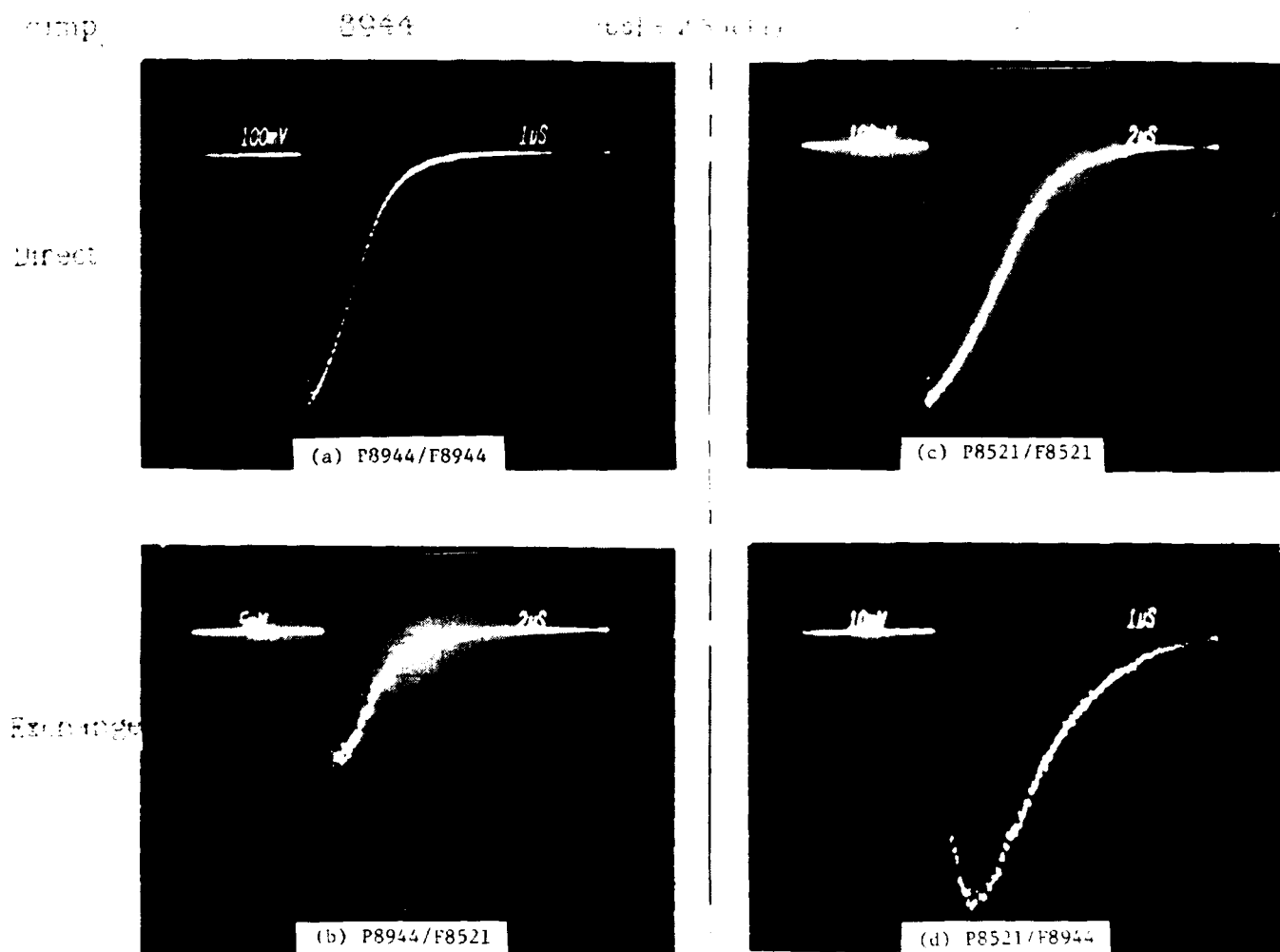


Figure 3.4 Oscilloscope traces of the direct and excitation transfer fluorescence signals observed at a cell temperature of 332 K and a reservoir temperature of 317 K, giving a Cs density of  $2.55 \times 10^{11} \text{ cm}^{-3}$ . The pump/fluorescence wavelengths are (a) 894 nm/894 nm, (b) 894 nm/852 nm, (c) 852 nm/852 nm, and (d) 852 nm/894 nm.

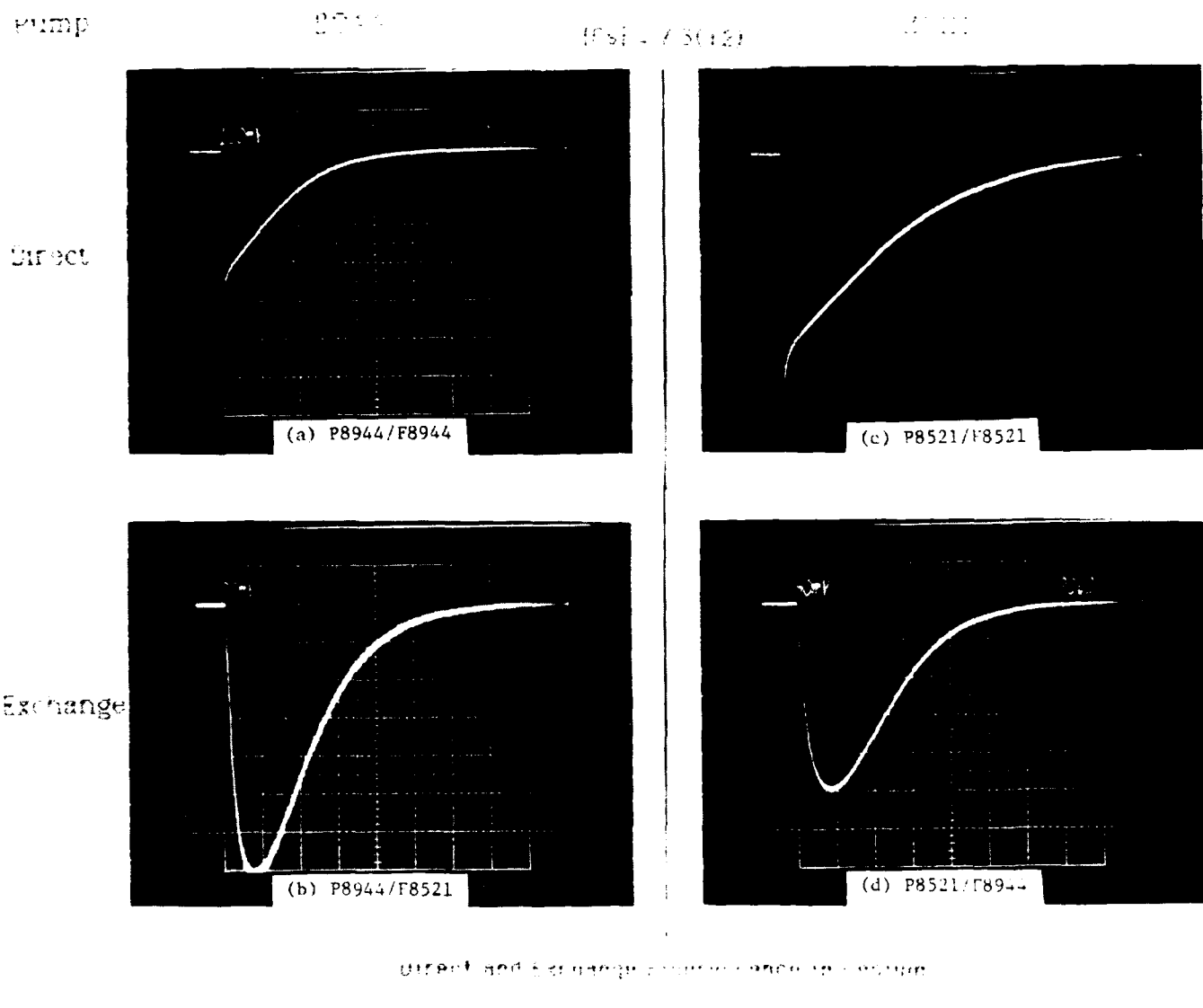
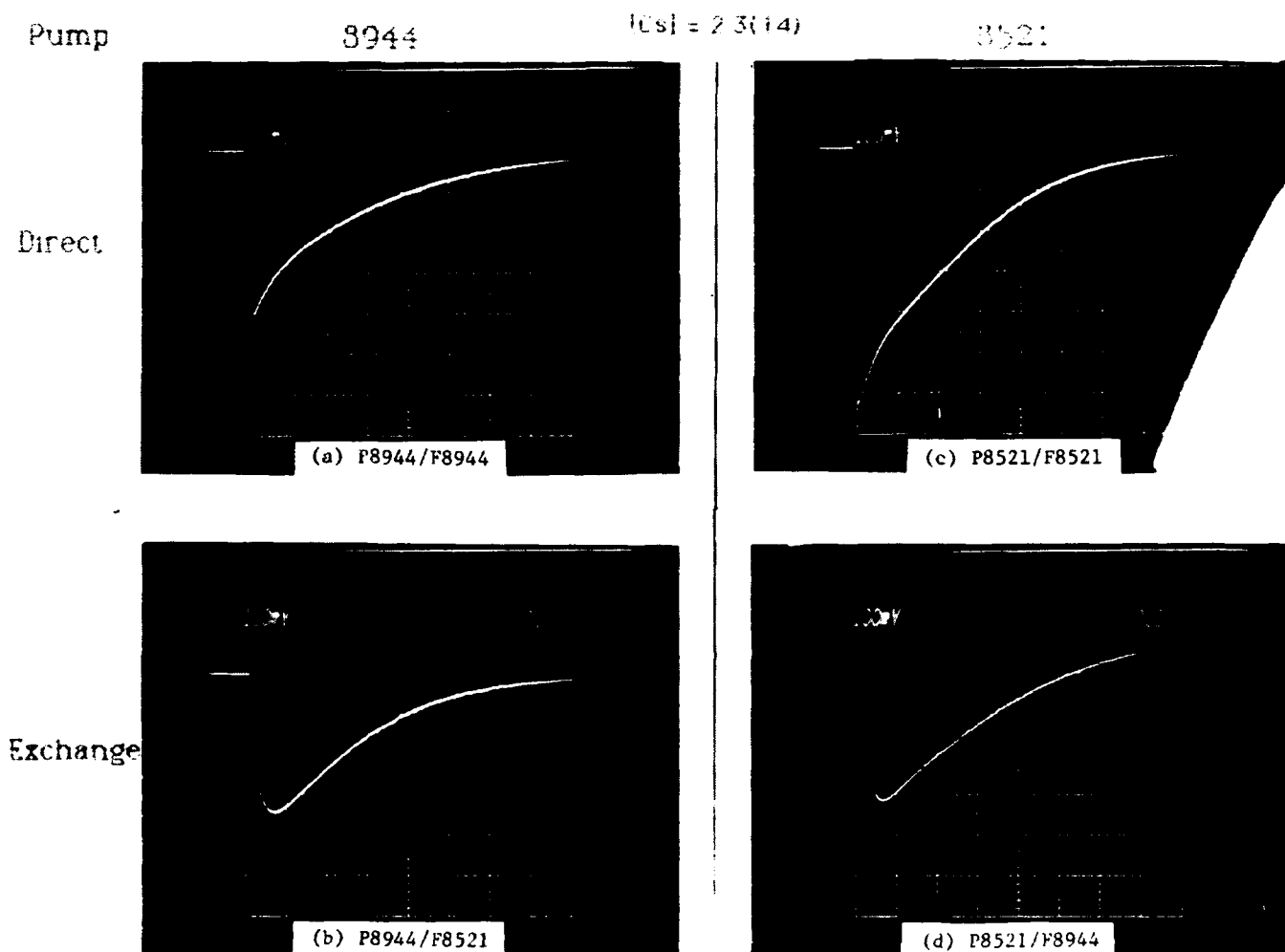


Figure 3.5 Oscilloscope traces of the direct and excitation transfer fluorescence signals observed at a cell temperature of 386 K and a reservoir temperature of 363 K, giving a Cs density of  $7.3 \times 10^{12} \text{ cm}^{-3}$ . The pump/fluorescence wavelengths are (a) 894 nm/894 nm, (b) 894 nm/852 nm, (c) 852 nm/852 nm, and (d) 852 nm/894 nm.



Direct and Exchange Fluorescence in Cesium

Figure 3.6 Oscilloscope traces of the fluorescence signals observed at a cell temperature of 457 K and a reservoir temperature of 427 K, giving a Cs density of  $2.3 \times 10^{14} \text{ cm}^{-3}$ . The pump/fluorescence wavelengths are (a) 894 nm/894 nm, (b) 894 nm/852 nm, (c) 852 nm/852 nm, and (d) 852 nm/894 nm.

Curve 751545-A

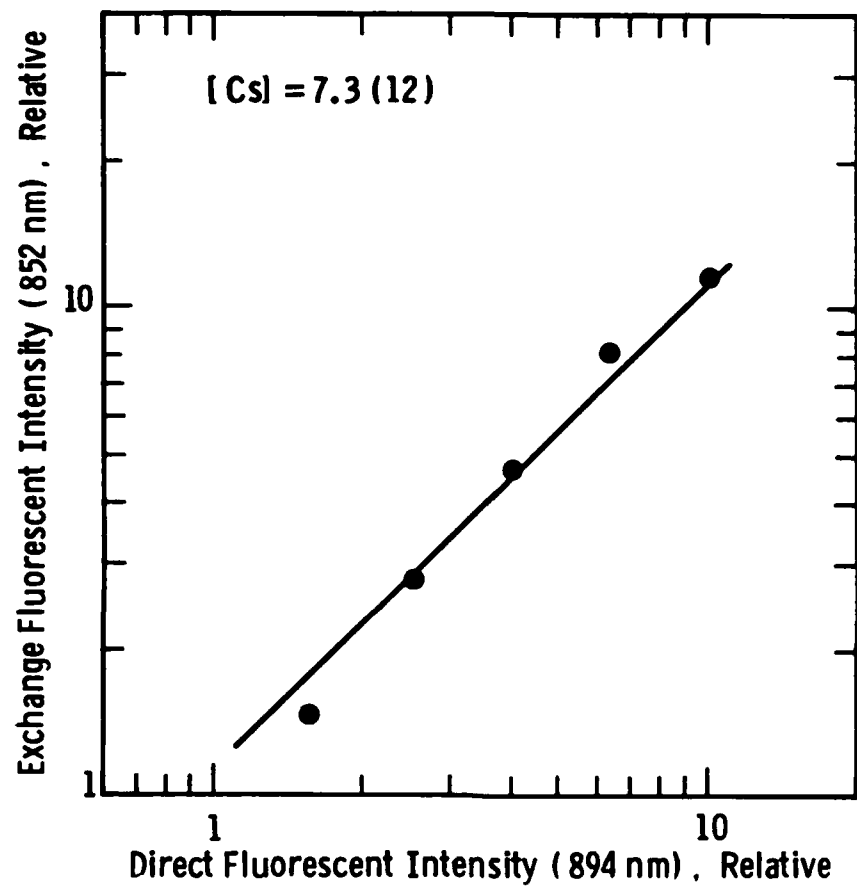


Figure 3.7 Correlation of direct (894 nm) and excitation transferred (852 nm) fluorescence at cesium density of  $7.3 \times 10^{12} \text{ cm}^{-3}$  and variable dye laser pulse energies.

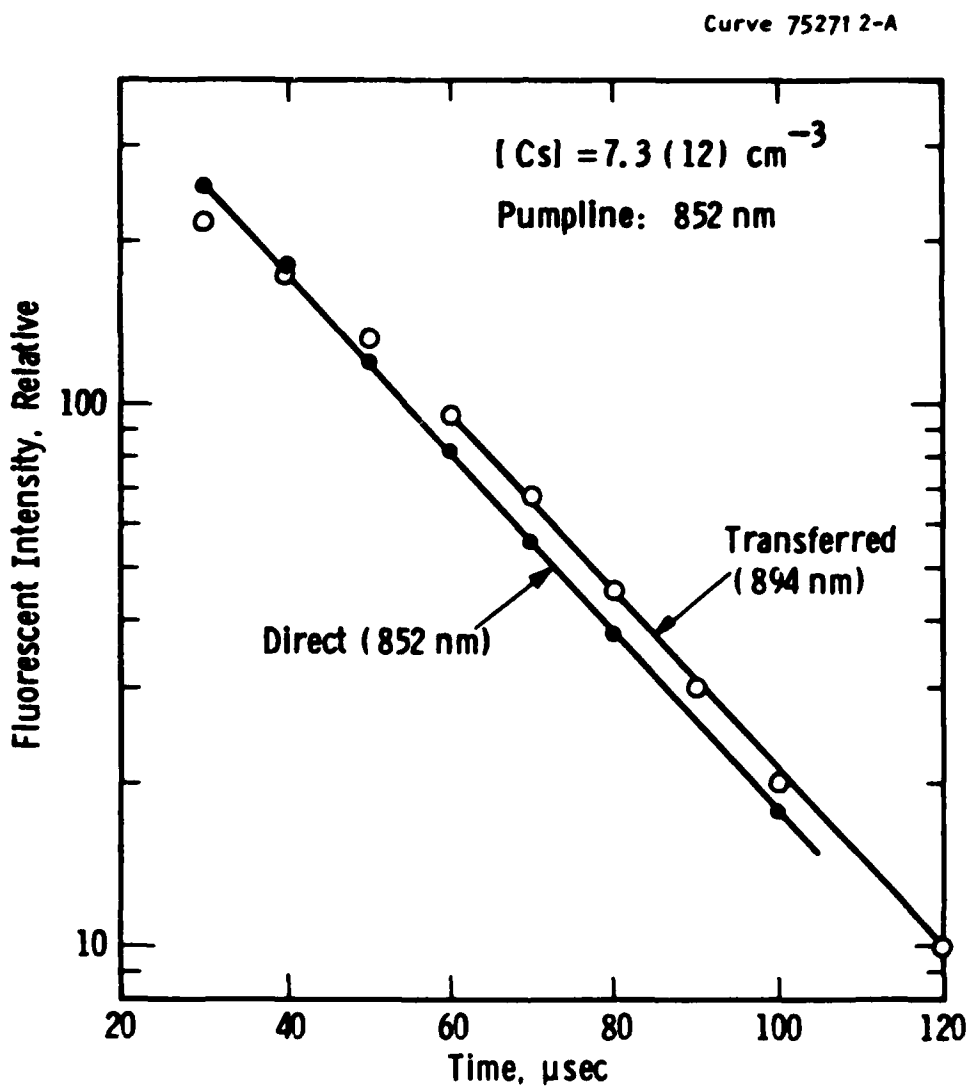


Figure 3.8 Semi-log plot of the direct (852 nm) and the excitation transferred (894 nm) fluorescence intensity versus time at late times after pulse excitation of the cesium vapor. The cesium vapor density is  $7.3 \times 10^{12} \text{ cm}^{-3}$ .

Curve 752713-A

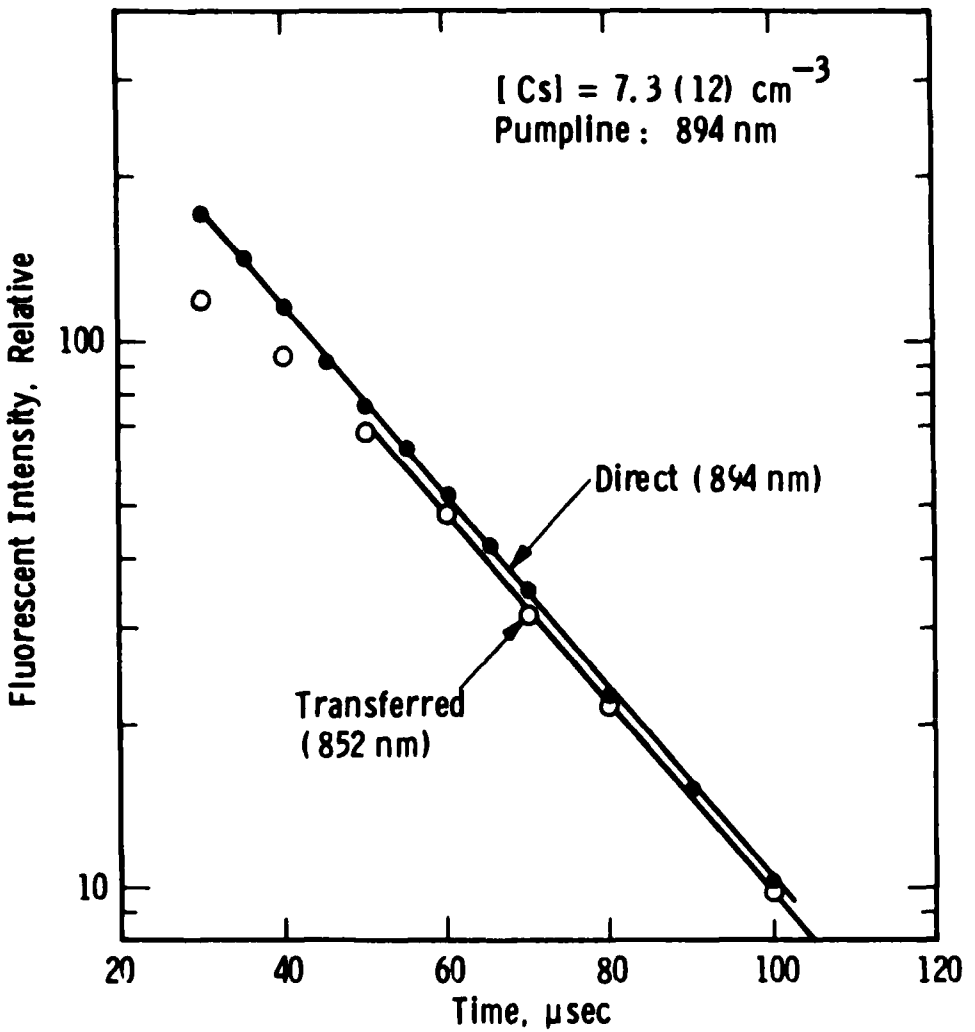


Figure 3.9 Semi-log plot of the direct (894 nm) and the excitation transferred (852 nm) fluorescent intensity versus time at late times after pulse excitation of the cesium vapor. The cesium vapor density is  $7.3 \times 10^{12} \text{ cm}^{-3}$ .

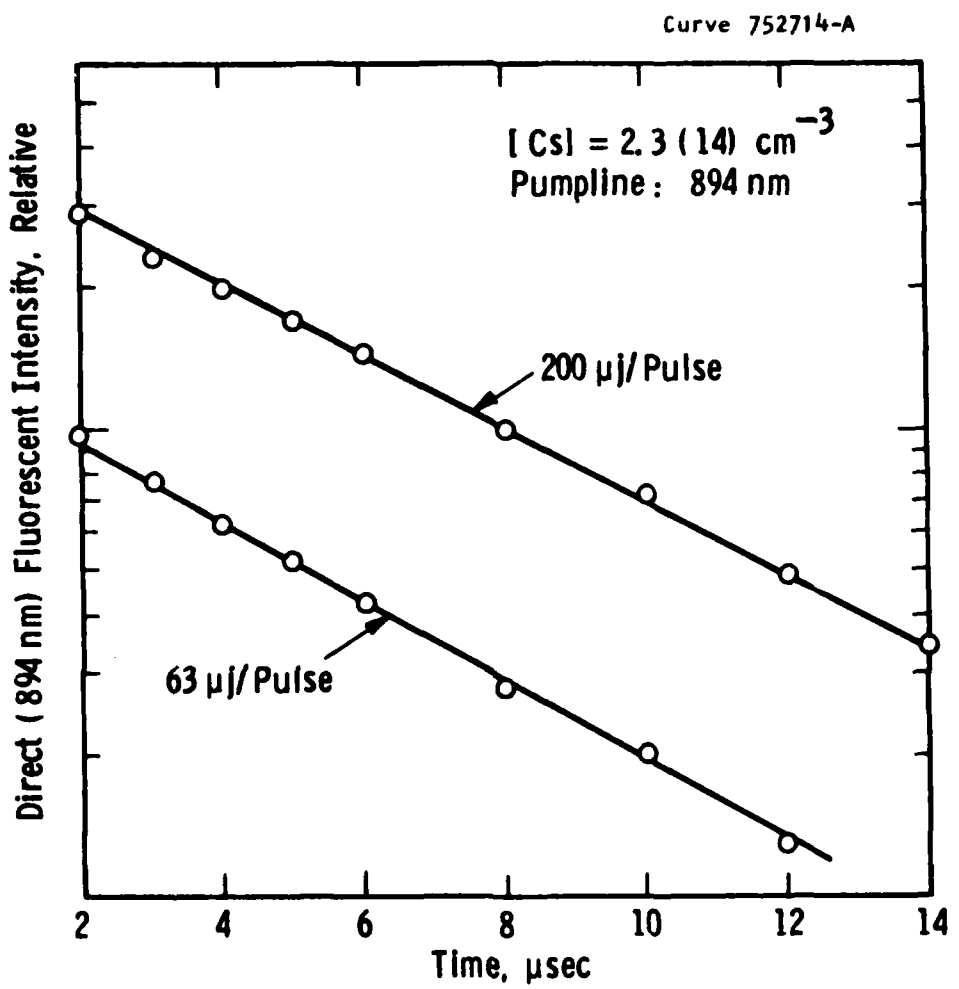


Figure 3.10 Semi-log plot of the direct (894 nm) fluorescence intensity versus time after pulse excitation of the cesium vapor at the two different dye laser pulse energies indicated. The cesium vapor density is  $2.3 \times 10^{14} \text{ cm}^{-3}$ .

and in general we see no significant dependence of the decay time constant on laser power.

The next section is devoted to the detailed analysis of the time dependent fluorescence from both the  $6P_{1/2}$  and  $6P_{3/2}$  states, taking into account the effects of hyperfine splitting, line shape, excitation exchange, and self-quenching.

### 3.4 DATA ANALYSIS

In this section we describe the steps involved in extracting the important basic parameters from the time dependent fluorescence measurements described in the previous section. We first present the general analytical solution for the three level system involved. The approach used to optimize the fitting of the double exponential functions to the data is then described. The dependence of the resulting two time constants on the cesium density is then fitted to a model which takes account of the collisional quenching of the resonance states and of trapping of the resonance radiation. The latter involves the transition from a predominantly Doppler broadened line to a predominantly collision broadened line, the treatment of which is further complicated by the presence of hyperfine components whose spacing is comparable to the line widths, depending on the Cesium density. The method used to represent this situation is described in a separate subsection. In the final subsection theory and experiment are reconciled by choosing appropriate values for the collisional energy exchange and quenching cross sections, which constitute the "unknowns" in the present study.

#### 3.4.1 Time Dependent Collisional Mixing Model

The situation to be analyzed is represented in Figure 3.11. The analysis has been presented by a number of previous authors [Rosser et al. (1969); Stephenson and Bradley Moore (1972); Yardley (1980)]. Therefore we give only an outline of the method. The notation employed here and elsewhere in this section is summarized in Table 3.2. The continuity equations for the populations of levels 1 and 2 are

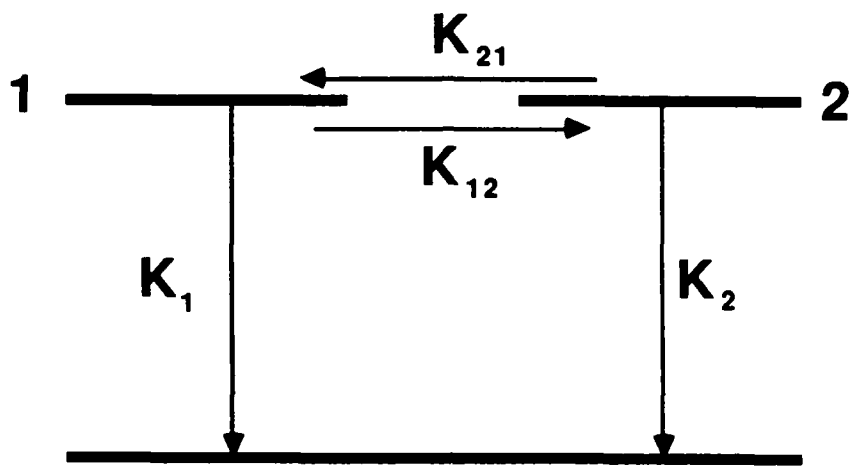


Figure 3.11 Three-level system considered in the analysis of the Cs fluorescence data.

$$\frac{dN_1}{dt} = -N_1(K_1 + K_{12}) + N_2 K_{21} \quad (3.15)$$

$$\frac{dN_2}{dt} = -N_2(K_2 + K_{21}) + N_1 K_{12}$$

These equations are solved straightforwardly by further differentiation and elimination of one or other of the variables. The resulting second order differential equation is then amenable to standard methods of solution. In the present context the solutions of interest satisfy the boundary condition that, at  $t=0$ , only one upper level has been populated. Designating this to be level 1, the subsequent behavior is given by

$$N_1(t)/N_1(0) = A_f \exp(-t/\tau_f) + A_s \exp(-t/\tau_s) \quad (3.16)$$

$$\text{and } N_2(t)/N_1(0) = A [\exp(-t/\tau_s) - \exp(-t/\tau_f)] \quad (3.17)$$

$$\text{where } A = K_{12}/(\tau_f^{-1} - \tau_s^{-1}) \quad (3.18)$$

$$A_f = (K_1 + K_{12} - \tau_s^{-1})/(\tau_f^{-1} - \tau_s^{-1}) \quad (3.19)$$

$$A_s = (\tau_f^{-1} - K_1 - K_{12})/(\tau_f^{-1} - \tau_s^{-1}) \quad (3.20)$$

$$\tau_f^{-1} = \frac{1}{2} \left\{ (K_1 + K_{12} + K_{21} + K_2) + [(K_1 + K_{12} - K_{21} - K_2)^2 + 4K_{12}K_{21}]^{1/2} \right\} \quad (3.21)$$

$$\tau_s^{-1} = \frac{1}{2} \left\{ (K_1 + K_{12} + K_{21} + K_2) - [(K_1 + K_{12} - K_{21} - K_2)^2 + 4K_{12}K_{21}]^{1/2} \right\} \quad (3.22)$$

Table 3.2 Listing the symbols used throughout Section 3 of this report, together with their definition, and the equation where each one is introduced or defined.

<u>Symbol</u>	<u>Description</u>	<u>Eqn.</u>
$a$	Voigt parameter, proportional to ratio of the collision broadened width to the Doppler width.	3.30
$A_{f,s}$	Amplitude of the fast, slow components of the double exponential decay.	3.16
$f$	Actual number of hyperfine components of the line	
$f_e$	Effective number of hyperfine components.	3.27
$F$	Total angular momentum quantum number of a hf level including nuclear spin.	3.46
$g$	Escape factor.	3.24
$g_c$	Escape factor in the presence of collision broadening alone.	3.25
$g_d$	Escape factor in the presence of Doppler broadening alone.	3.25
$g_{cd}$	Escape factor associated with Doppler absorption, collision emission.	3.25
$g_{u,l}$	Degeneracy of the upper, lower state.	3.31
$I$	Nuclear angular momentum quantum number.	3.46
$J$	Total angular momentum quantum number of orbital electrons including electron spin.	3.46
$k$	Boltzmann constant.	3.30
$k_o$	Absorption coefficient at line center, calculated assuming no hfs.	3.31
$k_i$	Absorption coefficient at line center for the $i$ 'th hyperfine component.	3.33
$K_{1,2}$	Net loss coefficient of level 1,2 to the ground state.	3.15
$K_{12}$	Loss coefficient of level 1 to level 2.	3.15
$K_{21}$	Loss coefficient of level 2 to level 1.	3.15

M	Mass of the Cs atom.	3.30
N	Total number density of Cs atoms.	3.30
$N_{1,2}$	Number density of Cs atoms in excited state 1,2.	3.15
R	Radius of the cylindrical container.	3.27
$t_p$	Time at which $N_2(t)$ maximizes.	3.23
$T_r$	Reservoir temperature, K.	3.51
$T_c$	Cell temperature, K.	3.30
$T(\rho)$	Transmission coefficient for optical depth $\rho$ .	3.32
$v_o$	Most probable atomic speed, $(2kT_c/M)^{1/2}$ .	3.36
$v_T$	Average center-of-mass thermal velocity.	3.49
$x_i$	Fractional relative intensity of the i'th hyperfine	3.32
$\Delta$	Separation of adjacent hyperfine components.	
$\lambda_o$	Wavelength at line center.	3.31
$\nu_o$	Optical frequency at line center.	3.35
$\sigma_{q1,2}$	Quenching cross section of level 1,2 to the ground state.	3.48
$\sigma_{12}$	Cross section for excitation transfer from level 1 to 2.	3.50
$\tau_c$	Effective lifetime due to collision broadening.	3.30
$\tau_{f,s}$	Time constant of the fast, slow components of the double exponential decay.	3.16
$\tau_n$	Natural radiative lifetime of the excited level.	3.13
$\psi_i$	Displacement from line center where $k_i R = 1$ . (Absorption half-width).	3.35
$\psi_c$	Absorption half-width of a collision broadened line.	3.37
$\psi_d$	Absorption half-width of a Doppler broadened line.	3.36

We note from Eq. (3.17) that  $N_2(t)$  peaks at time

$$t_p = \ln(\tau_s/\tau_f) / (\tau_f^{-1} - \tau_s^{-1}) \quad (3.23)$$

In the above the subscripts "f" and "s" indicate the fast and slow components of the double exponential behavior.

The solutions corresponding to pumping level 2 are obtained from the above by simply interchanging 1 and 2 in the various subscripts. This has no effect on  $\tau_f$  and  $\tau_s$ , and hence  $t_p$  is also unchanged. The ratio  $A_f/A_s$ , however, becomes equal to the reciprocal of its former value. We conclude that, irrespective of the level originally pumped, the time dependent fluorescence of both levels 1 and 2 can yield three primary quantities:  $\tau_f$ ,  $\tau_s$  and the ratio  $A_f/A_s$ . In practice it is possible to extract the ratio  $A_f/A_s$  with useful accuracy only when its value is reasonably close to unity, and  $\tau_f$  and  $\tau_s$  are substantially different.

### 3.4.2 Curve Fitting to $N_1(t)$ and $N_2(t)$

The procedure adopted to extract the values of  $\tau_f$  and  $\tau_s$  from the digitized measured fluorescence measurements is simpler to apply in the case of the  $N_2(t)$  data, since in this case the data and the fitted curve can both be normalized to the peak value, and the problem reduces to one of simply fitting the shape. This was done with an interactive screen plotting routine using commercially available software on a personal computer. Having digitized the data, it consisted of a sequence of points. For each such point a corresponding fitted point is calculated using the current best estimate of  $\tau_f$  and  $\tau_s$ , with the resulting curves being displayed automatically in both linear and logarithmic form. The program also tracks the standard deviation between the data and the fit, calculated in terms of their logarithms. In seeking the best fit the values of  $\tau_f$  and  $\tau_s$  were allowed to assume any values satisfying the constraint  $\tau_f < \tau_s$ . The convergence to the

best values was achieved with the help of a routine which allowed one or other, or both of these to be varied in a prescribed sequence, and halted at the local minimum in the standard deviation of the data from the fitted curve. In the final optimization small adjustments were allowed in the zero of the time scale attached to the data by the digitization procedure.

The same general procedure was applied to the fitting of  $N_1(t)$  data except that in this case it was also necessary to fit the amplitude normalization.

Examples of both types of fitted data are shown in Figure 3.12. The values of  $\tau_f$  and  $\tau_s$  used to compute each fitted curve are indicated in the figure. Also indicated is the quality of the fit as measured by the standard deviation, quoted here as a percentage. In the examples of  $N_1(t)$  type data the ratio  $A_f/A_s$  given by the fit is also indicated on the figure. Note that the four curves shown in Figure 3.12 constitute a set, in that all four correspond to the same set of experimental conditions of reservoir and cell temperatures. Thus in principle they should all give the same values for  $\tau_f$  and  $\tau_s$ , and the product of the two values of the ratio  $A_f/A_s$  should be unity. For purposes of further analysis we simply calculate the mean values of  $\tau_f$  and  $\tau_s$  and regard these as representative of the measurements at these particular conditions.

The various sets of data corresponding to other temperatures were treated in the same way, giving in all 18 pairs of values of  $\tau_f$  and  $\tau_s$  corresponding to Cesium densities ranging from  $1.1 \times 10^{11}$  to  $2.3 \times 10^{14} \text{ cm}^{-3}$ . This data is used in Section 3.4.4 to determine the relevant collision cross sections controlling the effective lifetimes at the higher densities. Before proceeding to such an analysis, however, we must first establish an appropriate method for calculating the effective radiative lifetimes of the two upper states under the present conditions where the resonance radiation from each state only escapes from the system after a sequence of absorption-reemission events. This is discussed in the next subsection.

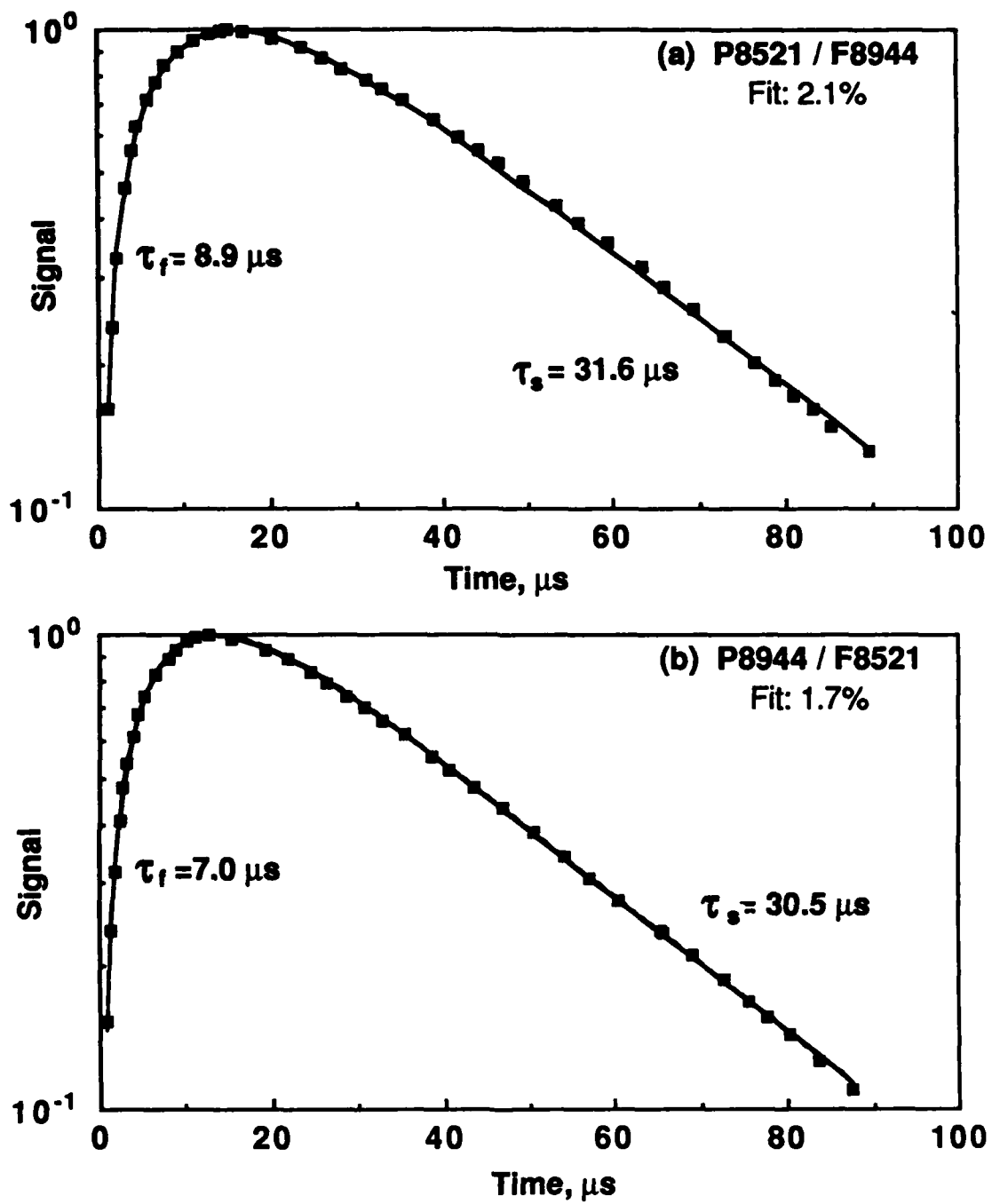


Figure 3.12 (a) & (b). Example set of double exponential fits to the digitized oscilloscope traces, taken at a Cs density of  $1.36 \times 10^{13} \text{ cm}^{-3}$ . On each graph the points represent the digitized data, and the curve is the theoretical fit having the time constants indicated. The pump/fluorescence wavelengths are shown in each case, and the standard deviation between the data and the fit is given as a percentage.

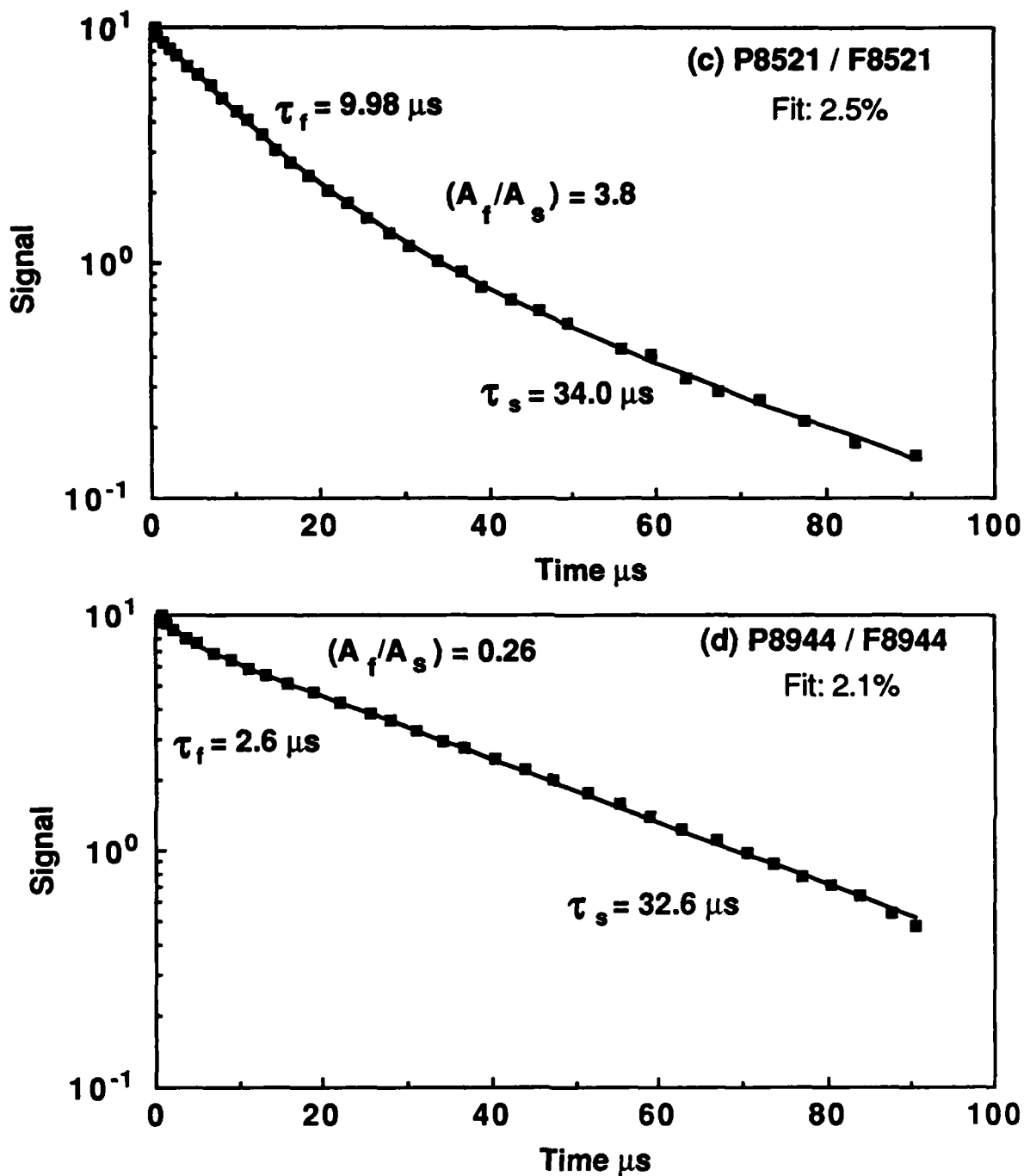


Figure 3.12 (c) & (d). Example set of double exponential fits to the digitized oscilloscope traces, taken at a Cs density of  $1.36 \times 10^{13} \text{ cm}^{-3}$ . On each graph the points represent the digitized data, and the curve is the theoretical fit having the time constants indicated. The pump/fluorescence wavelengths are shown in each case, and the standard deviation between the data and the fit is given as a percentage.

### 3.4.3 The Transport of Resonance Radiation

The basic theory of the transport of imprisoned resonance radiation was first developed independently by Holstein (1947, 1951) and by Biberman (1947). The theory has subsequently been further refined by a number of authors, and relevant references may be found in the papers of Irons (1979 a,b,c). Here we shall draw primarily on the work of Walsh (1959).

#### 3.4.3.1 The Escape Factor, $g$

It was shown by Holstein (1947) that the decay of the density of excited states within an enclosure may be represented by the superposition of the eigenmodes characteristic of the enclosure shape. In the absence of an external source of further excitation the spatial form of the excited state density rapidly approaches that of the lowest eigenmode, and the subsequent local rate of change of excited state density  $N^*$  may be represented simply by

$$\frac{dn^*}{dt} = -gN^*/\tau_n \quad (3.24)$$

where  $g$  is the "escape factor" associated with the lowest order decay mode. The value of  $g$  depends on the shape of the container, on the size of the container measured in terms of the optical depth, and on the line shapes for emission and absorption. These quantities depend in turn on the number density of participating atoms, and on their temperature. Asymptotic expressions for  $g$ , appropriate for large optical depths, were calculated approximately by Holstein for the separate cases of Doppler and collision broadening, for plane parallel slab and infinite cylinder geometries. Subsequent more detailed calculations, summarized by Irons (1979b) have shown these expressions to be accurate to within a few percent. In the present problem however the range of densities covered is such that we must in general take into account the combined effects of both Doppler and collision broadening, and in addition we must

recognize that at the lowest densities the asymptotic form for  $g$  will be inaccurate, and must in some way be modified.

The problem of including the effects of both Doppler and collision broadening in the calculation of  $g$  was addressed by Walsh (1959). His analysis led him to propose the interpolation formula

$$g = g_d \exp(-g_{cd}^2/g_c^2) + g_c E_2(g_{cd}/g_c) \quad (3.25)$$

where  $E_2$  is the error integral. The subscripts "c," "d," and "cd" refer respectively to the escape factors applicable to a collision broadened line, a Doppler broadened line, and an equivalent escape factor representing the effect of events involving Doppler absorption followed by emission in the relatively transparent collision dominated wings.

Walsh's interpolation formula was used by Zollweg, Liebermann and McLain (1981) in a slightly modified form. These authors also introduced modifications to the asymptotic forms for  $g_d$  and  $g_{cd}$  such that their values tended to unity for small optical depths. Based on this work we have used the following formula:

$$g = g_d \exp(-g_{cd}^2/g_c^2) + (g_{cd}^{-3} + g_{cc}^{-3})^{-1/3} \quad (3.26)$$

where  $g_d = 1.60/\{1.60 + (k_o R/f_e)[\pi \ln(1 + k_o R/f_e)]^{1/2}\} \quad (3.27)$

$$g_c = \exp(-k_o R/f_e a \pi^{1/2}) I_o(k_o R/f_e a \pi^{1/2}) \quad (3.28)$$

$$g_{cd} = a/\{a + (\pi/2)[\pi \ln(1 + k_o R/f_e)]^{1/2}\} \quad (3.29)$$

$$a = (1/N\tau_c)(\lambda_o N/4\pi)(M/2kT_c)^{1/2} \quad (3.30)$$

$$k_o = (\lambda_o^3 N / 8\pi^{3/2}) (g_u/g_l) (1/\tau_n) (M/2kT_c)^{1/2} \quad (3.31)$$

These equations differ from those of Zollweg et al. (1981) in three respects. The major change is that the effects of natural broadening are omitted from the definition of the Voigt parameter "a", proportional to the ratio of the collision broadened width to the Doppler width. This change is largely pragmatic, in that we then find the interpolation formula, Eq. (3.26) or Eq. (3.25) to be better behaved in the region  $k_o R \approx 1$  and lower, and in the transition between the regions of predominantly Doppler broadening and collisional broadening. The omission of natural broadening effects can be rationalized on the basis of the anticipated incomplete frequency redistribution in the natural wing, as discussed by Huennekens and Gallagher (1983).

The interpolation formula, Eq. (3.25) or Eq. (3.26), is the original form proposed by Walsh (1959). We find the modification made by Zollweg et al. (1981), to control the asymptotic value of  $g$  as  $k_o R$  becomes very small, to be unnecessary provided we use the modified definition of the Voigt parameter given in Eq. (3.30).

The remaining difference lies in the constant chosen for Eq. (3.27). Zollweg et al. (1981) used a value of 1.82 for consistency with the results of Phelps and McCoubrey (1960) for  $5 < k_o R < 400$ , which are approximately 20% larger than are given by Holstein's asymptotic formula. We find, however, that use of the value 1.60 gives better agreement at low  $k_o R$  values with the results of Blickensderfer et al. (1976), and clearly will give the correct asymptotic limit at large values of  $k_o R$ .

Evaluation of Eq. (3.26), and the associated Eqs. (3.27) through (3.31), proceeds separately for the two resonance lines involved in the present context. For the natural lifetimes we use the values  $\tau_n(6^2P_{1/2}) = 34$  ns and  $\tau_n(6^2P_{3/2}) = 30.5$  ns (Link, 1986; Gallagher, 1967). For the density normalized collisional broadening frequencies we use the values  $(1/N\tau_c)_{1/2} = 8.6 \times 10^{-8} \text{ s}^{-1}$  and  $(1/N\tau_c)_{3/2} =$

$1.51 \times 10^{-7} \text{ s}^{-1}$ , given by Chen and Phelps (1968). The values used for  $f_e$ , the effective number of hyperfine components, were deduced from considerations of the ratio of the separations of the components to the trapped width of the individual components, as discussed in the next subsection.

#### 3.4.3.2 The Effective Number of Hyperfine Components, $f_e$

In many instances the radiation of a given line consists of a number of closely spaced but distinct components due to the presence of various isotopes and/or hyperfine splitting of the level arising from the interaction of the orbital electrons with the nuclear spin. Cesium has only one stable isotope so we are concerned here only with the latter effect.

In the simplest possible case, where the line consists of "f" equally intense components, separated sufficiently from each other that the levels do not exchange energy radiatively, the effect of the hyperfine structure on the radiative transport is accounted for by simply dividing the optical depth  $k_o R$  by the number of components,  $f$ . In effect, each line component "sees" an absorber density of  $N/f$ . At the other extreme, where the separation of the components is much smaller than the line widths, the line structure has no effect on the process of radiation transport. In general, however, the situation is more complicated, due to the partial overlap of some or all of the components, and also to a lesser degree by the fact that different components have different relative intensities. For present purposes we take account of this complication through the use of an effective number of components, represented by the factor  $f_e$  in the equations given in the previous subsection. To estimate  $f_e$  we use the same general approach as was employed by Walsh (1959), without the level of detailed calculation which he performed for mercury.

Following Holstein (1947), we note that for a multicomponent line the net transmission coefficient may be written

$$T(\rho) = \sum x_i T_i(\rho) \quad (3.32)$$

where  $\rho$  is distance,  $x_i$  is the intensity of the  $i$ 'th component, and  $\sum x_i = 1$ .  $T_i(\rho)$  is the transmission coefficient for the  $i$ 'th component, for which

$$k_i = x_i k_o \quad (3.33)$$

For the purpose of this discussion we assume sufficiently large values of  $k_i \rho$  at line center for the asymptotic forms given by Holstein to apply for each isolated component. For example, when Doppler broadening dominates

$$T_i(\rho) = (1/k_i \rho) (1/\pi \ln k_i \rho)^{1/2} \quad (3.34)$$

To estimate  $T_i(\rho)$  for a particular component in the presence of adjacent components we must consider the extent to which the lines overlap. The escape of radiation from a particular line occurs at wavelengths sufficiently displaced from line center that  $k_i \rho \leq 1$ . Other wavelengths, within the absorbing core are essentially trapped. Following Walsh (1959) we define an absorption half-width  $\Phi_i$  for each component by

$$k_i(\nu_o + \Phi_i) = 1 \quad (3.35)$$

For a Doppler broadened line we obtain

$$\Phi_d = (\nu_o / \lambda_o) (\ln k_o \rho / f)^{1/2} \quad (3.36)$$

while for a collision broadened line we have

$$\Psi_c = (v_o/\lambda_o) (a k_o \rho / f \pi^{1/2})^{1/2} \quad (3.37)$$

We may discuss the degree of overlap of lines separated by  $\Delta$  in terms of the ratio  $\Delta/\Psi$ .

Lines Completely Isolated,  $\Delta \gg \Psi$

Under these conditions use of Eq. (3.32) is straightforward, giving in the case of Doppler broadening

$$T_d(\rho) = \sum [1/\rho k_o (\pi \ln x_i k_o \rho)^{1/2}] \quad (3.38)$$

This may be written in the form

$$T_d(\rho) = C(\rho k_o / f)^{-1} [\pi \ln(\rho k_o / f)]^{-1/2} \quad (3.39)$$

where  $C = f^{-1} [\ln(\rho k_o / f)]^{1/2} \sum [\ln(\rho x_i k_o)]^{1/2}$  (3.40)

is close to unity, and is identically so when the  $f$  components are of equal intensity, i.e. when  $x_i = f^{-1}$ , all  $i$ .

Similarly, for isolated collision broadened components we obtain

$$T_c(\rho) = [a/\pi^{1/2} \rho (k_o/f)]^{1/2} \sum (x_i/f)^{1/2} \quad (3.41)$$

where the sum is close to unity and again is identically so when the  $f$  components are of equal intensity. Hence, to a good approximation, the transmission coefficient for a line consisting of  $f$  isolated components is obtained from the appropriate form for a single line by using  $k_o/f$  in place of  $k_o$ . Therefore, in this situation we assume the effective number of components,  $f_e$ , to be equal to the actual number of components,  $f$ .

Partially Overlapping Lines,  $\Psi < \Delta \leq 2\Psi$

In this situation only the red wing of the reddest component and the blue wing of the bluest component contribute significantly to  $T(\rho)$ , and hence

$$T(\rho) = \frac{1}{2} [x_1 T_1(\rho) + x_f T_f(\rho)] \quad (3.42)$$

where  $T_1(\rho)$  and  $T_f(\rho)$  are the values which would apply to these components if they were isolated. For Doppler broadened lines these are given by Eq. (3.34), and hence we obtain from Eq. (3.42)

$$T_d(\rho) = C_1 / [\rho k_o (\pi \ln \rho k_o)^{1/2}] \quad (3.43)$$

$$\text{where } C_1 = \frac{1}{2} (\ln \rho k_o)^{1/2} [(\ln x_1 \rho k_o)^{-1/2} + (\ln x_f \rho k_o)^{-1/2}] \quad (3.44)$$

$$\approx [\ln \rho k_o / \ln (\rho k_o / f)]^{1/2}$$

Thus the factor  $C_1$  is in general  $> 1$ , and tends to unity for large  $\rho k_o$ , when Eq. (3.43) gives the value appropriate for complete overlap of all the components. Therefore in this situation we expect the effective number of components,  $f_e$ , to be in the range  $1 \leq f_e < f$ .

For collision broadened lines Eq. (3.42) gives

$$T_c(\rho) = [a / \pi^{1/2} \rho k_o]^{1/2} [\frac{1}{2} (x_1^{1/2} + x_f^{1/2})] \quad (3.45)$$

$$= [a / \pi^{1/2} \rho k_o f]^{1/2} \quad \text{when } x_i = f^{-1}, \text{ all } i.$$

We note that, in this region (i.e. partial overlap of collision broadened lines) the transmission coefficient is lower than the value it would attain with complete overlap, approximately by the factor  $f^{-1/2}$ .

The effective number of components,  $f_e$ , is therefore predicted to go through a minimum value of  $f^{-1}$  before approaching unity when the lines completely overlap.

The hyperfine structure relevant to the present problem is shown in Figure 3.13 for the 8944 Å line, and in Figure 3.14 for the 8521 Å line. The hyperfine energies have been calculated from the standard equation (Arimondo et al. 1977, Eq. 2.7)

$$\Gamma(F) = \frac{1}{2} AK + B[(3/2)K(K+1) - 2I(I+1)J(J+1)]/2I(2I-1)2J(J-1) \quad (3.46)$$

where

$$K = F(F+1) - I(I+1) - J(J+1)$$

using the values of A and B recommended for Cs in the same reference, namely

$$A(6P_{1/2}) = 291.90 \text{ MHz}; A(6P_{3/2}) = 50.34 \text{ MHz}; B(6P_{3/2}) = -0.38 \text{ MHz}$$

In Figures 3.13 and 3.14 the fractional relative intensities are also indicated. The values shown were obtained from the tables of White and Eliason (1933).

The values of  $\Psi_d$  and  $\Psi_c$  have been calculated using Eqs. (3.36) and (3.37) for each set of experimental conditions. The values of  $\Psi_d$ , calculated using the actual values of  $f$ , range from 251 to 783 MHz for the 8944 Å line, and from 291 to 841 MHz for the 8521 Å line. We note that the components of the 8944 Å line begin to overlap due to Doppler broadening only at the highest densities. Therefore, in computing  $g_d$  from Eq. (3.27), and  $g_{cd}$  from Eq. (3.29), we have assumed a value of  $f_e(8944) = 4$  at low densities, and reduced its value at higher densities according to the algorithm

$$f_e(8944) = 4 / \left[ 1 + \Psi_d(8944) / 1168 \right] \quad (3.47)$$

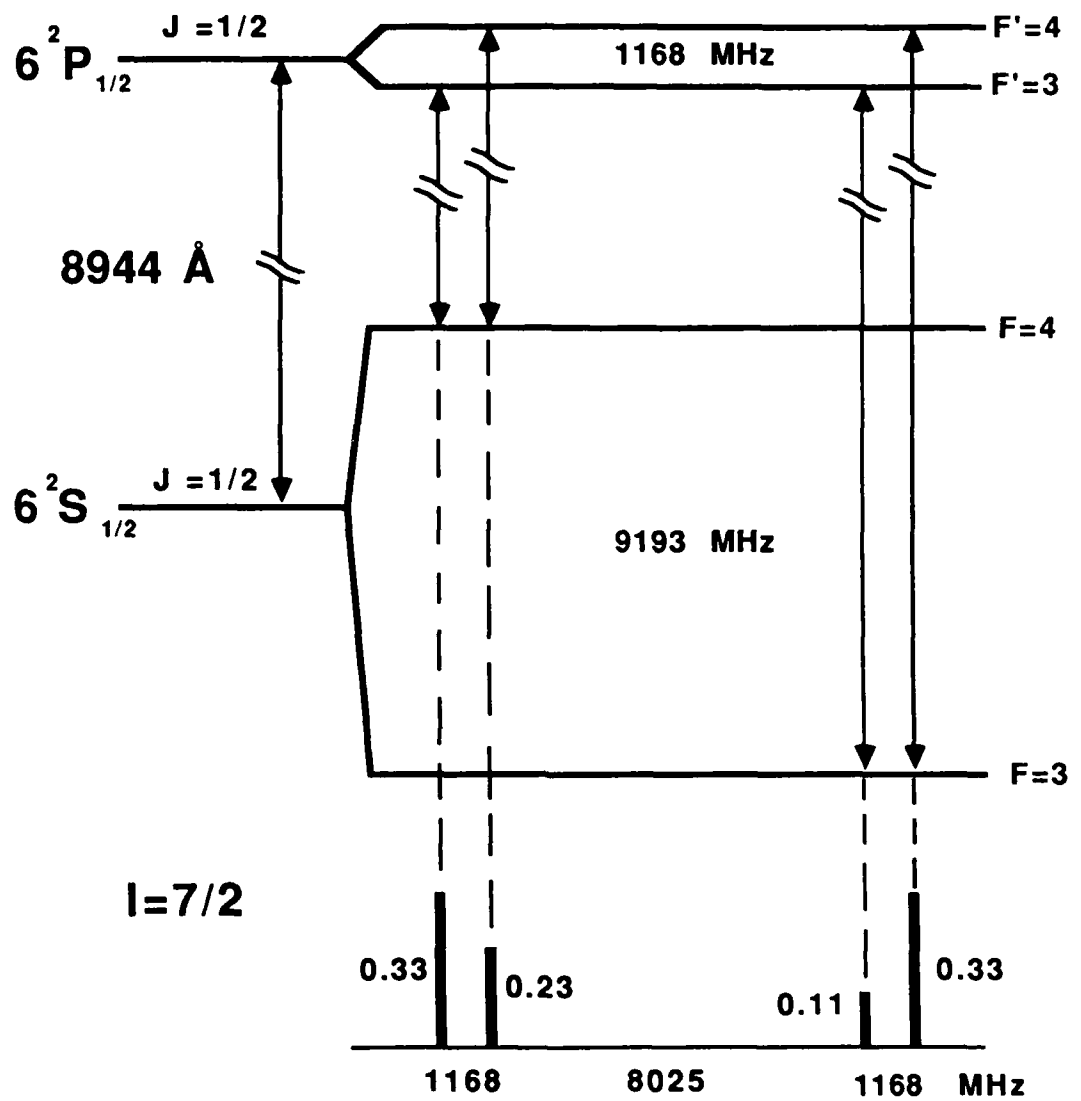


Figure 3.13. The hyperfine levels of the  $6^2S_{1/2}$  and  $6^2P_{1/2}$  states of Cs, and the resulting hyperfine structure of the  $8944 \text{ \AA}$  line. The separation and relative weights of the four components are shown in the lower right portion of the figure.

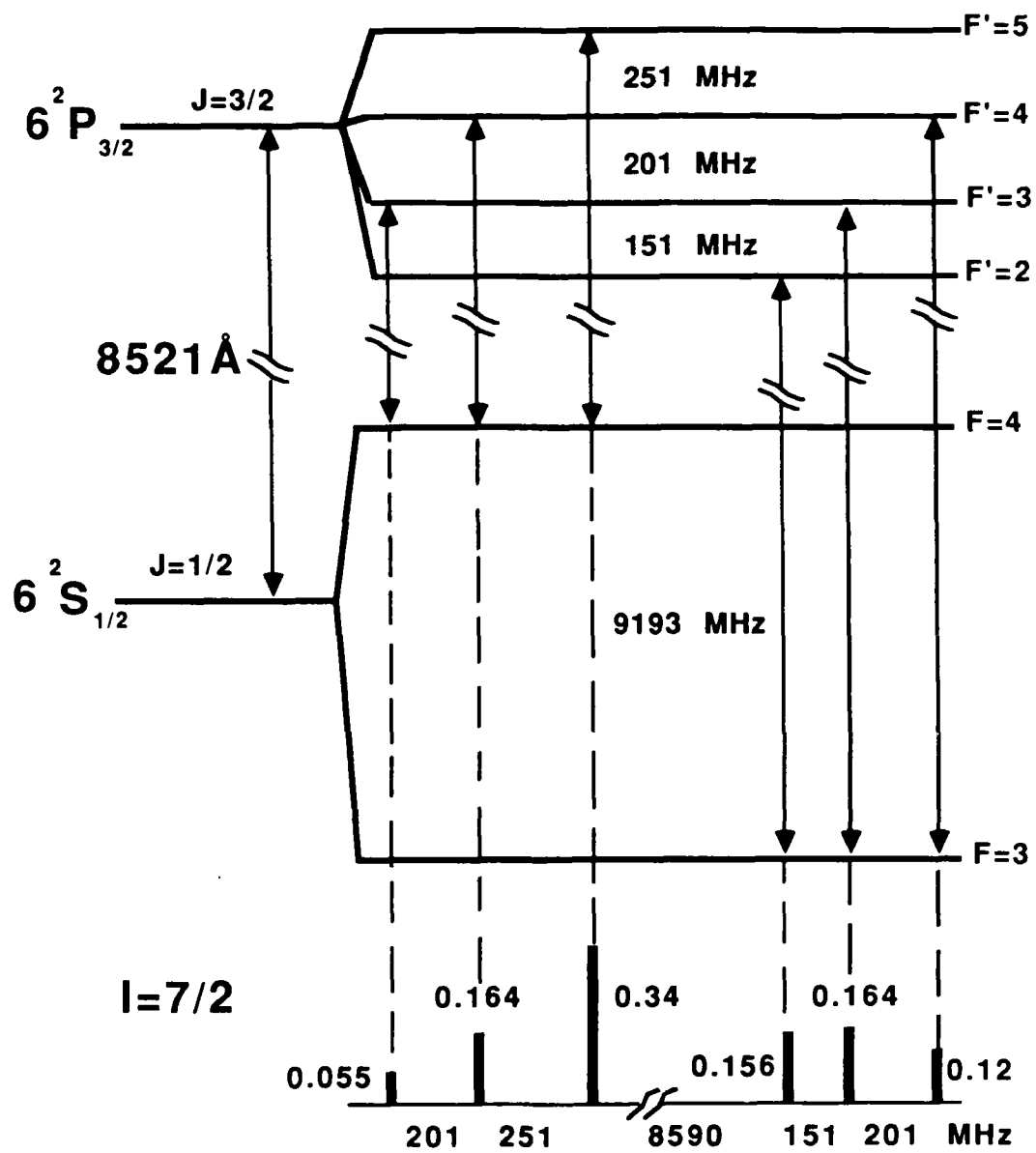


Figure 3.14 The hyperfine levels of the  $6^2S_{1/2}$  and  $6^2P_{3/2}$  states of Cs, and the resulting hyperfine structure of the 8521 Å line. The separation and relative weights of the four components are shown in the lower right portion of the figure.

In computing  $\Psi_c(8944)$  from Eq. (3.37) we have used  $f_e = 4$  throughout. The resulting values range from 0.6 to 1201 MHz. When evaluating  $g_c(8944)$  from Eq. (3.28), we have used for  $f_e(8944)$  the value 4 when  $\Psi_c(8944) < 584$  MHz, and the value 2 otherwise.

The six components of the 8521 Å line form two distinct groups, and the three components of each group overlap even at the lowest density. Therefore, in computing  $g_c(8521)$  and  $\Psi_c(8521)$  we have used a value of  $f_e(8521) = 2$  throughout. The values of  $\Psi_c(8521)$  computed from Eq. (3.37) range from 1.6 to 3231 MHz. Hence, as the density is increased  $f_e(8521)$  will range from 6 to approximately 1/2, the latter number arising from the partial overlap of two lines, each of which consists of three completely overlapping components. However, over the range where collision broadening is important the effective value of  $f_e(8521)$  is 2, and for simplicity we have assumed this value throughout. These choices of  $f_e$  are summarized in Table 3.3.

Table 3.3 Showing the values chosen for  $f_e$ , the effective number of hyperfine components, in calculating the quantities indicated. See Figures 3.13 and 3.14, and text for discussion.

Line	f	<u>Values of <math>f_e</math> used to calculate:</u>				
		$\Psi_d$	$\Psi_c$	$g_d$	$g_{cd}$	$g_c$
8521	6	6	2	2	2	2
8944	4	4	4	4+2	4+2	4+2

#### 3.4.4 Reconciling Computed and Measured Values of $\tau_f$ and $\tau_g$

Values of  $\tau_f$  and  $\tau_g$  are calculated using Eqs. (3.21) and (3.22) respectively. In so doing the value of  $K_1$  is computed from the equation

$$K_1 = g_1/\tau_{nl} + v_T N \sigma_{q1} \quad (3.48)$$

where  $g_1$  is computed as discussed in the preceding subsection,  $\sigma_{q1}$  is the self quenching cross section for level 1, treated here as an adjustable input parameter, and  $v_T$  is the average center-of-mass thermal velocity, given by

$$v_T = 4(kT_c/\pi M)^{1/2} \quad (3.49)$$

A similar equation to Eq. (3.48) applies for computation of  $K_2$ , with  $\sigma_{q2}$  being treated as an adjustable input parameter. The values of  $K_{12}$  and  $K_{21}$  are computed by assuming a trial value for the exothermic cross section, and calculating the endothermic cross section from detailed balancing. For example, in the case where  $\nu_1 > \nu_2$  we assume a temperature independent trial value for  $\sigma_{12}$  and use

$$\sigma_{21}/\sigma_{12} = (g_1/g_2) \exp[-h(\nu_1 - \nu_2)/kT_c] \quad (3.50)$$

to calculate the corresponding trial value of  $\sigma_{21}$ . Multiplying these cross sections by  $Nv_T$  then gives  $K_{12}$  and  $K_{21}$  respectively. The Cesium atomic density  $N$  is given by the relationship (Taylor and Langmuir, 1937)

$$\log_{10}[NT_c/9.668 \times 10^{18}] = 11.0531 - (4041/T_r) - \log_{10}T_r \quad (3.51)$$

In order to judge the overall quality of the fit of the theory to the experiment, and as an aid in optimizing the choice of the fitting parameters  $\sigma_{12}$ ,  $\sigma_{q1}$ , and  $\sigma_{q2}$ , we used commercially available software to compute and screen-plot the values of  $\tau_f$  and  $\tau_s$  as functions of the computed Cesium density, together with the measured values determined by the method described in subsection 3.4.2. This allowed trial-and-error fitting to proceed rapidly.

It was found possible to fit the measured values of  $\tau_f$  and  $\tau_s$  with any value of  $\sigma_{12} \leq 1.4 \times 10^{-13} \text{ cm}^2$ , by appropriately adjusting  $\sigma_{q1}$  and  $\sigma_{q2}$ . The limiting sets of cross sections are: ( $\sigma_{12} = 1.4 \times 10^{-13} \text{ cm}^2$ ,  $\sigma_{q1} = 0$ , and  $\sigma_{q2} = 3 \times 10^{-14} \text{ cm}^2$ ), and ( $\sigma_{12} = 0$ ,  $\sigma_{q1} = 2 \times 10^{-13} \text{ cm}^2$ , and  $\sigma_{q2} = 2 \times 10^{-14} \text{ cm}^2$ ). In order to further constrain the range of acceptable values we have also attempted to fit the measured relative signal strengths of the direct and transferred fluorescence signals. For convenience we choose to do this at the instant of the peak in the transferred fluorescence signal, given by Eq. 3.23. The ratio of the signal strengths is given by

$$\frac{S_2}{S_1} = \frac{N_2(t_p)}{N_1(t_p)} \cdot \frac{\lambda_1}{\lambda_2} \cdot \frac{\tau_{n1}}{\tau_{n2}} \cdot \frac{g_2}{g_1} \quad (3.52)$$

Where

$$\frac{N_2(t_p)}{N_1(t_p)} = K_{12} \left\{ \frac{\exp(-t_p/\tau_s) - \exp(-t_p/\tau_f)}{(K_1 + K_{12} - \tau_s^{-1}) \exp(-t_p/\tau_f) - (K_1 + K_{12} - \tau_f^{-1}) \exp(-t_p/\tau_s)} \right\} \quad (3.53)$$

is the ratio of the densities of the two excited states, and  $g_{1,2}$  are calculated as discussed in Section 3.4.3. These equations apply to the case where level 1 is pumped and the signal from level 2 peaks at time  $t_p$ . The corresponding equations for the case where level 2 is pumped are obtained by simply interchanging the subscripts. The signal ratios predicted in this way are compared to the measured ratios corrected for the wavelength dependence of the photomultiplier sensitivity, and the differing transmissions of the interference filters used to isolate the recorded signals.

The best fit to the measured signal ratios is obtained with  $\sigma_{12} = 1.3 \times 10^{-13} \text{ cm}^2$ , and  $\sigma_{q1} = \sigma_{q2} = 2 \times 10^{-14} \text{ cm}^2$ , shown in Fig. 3.15. The fit to the measured values of  $\tau_f$  and  $\tau_s$  achieved with these values of the cross sections is shown in Fig. 3.16. This cross section set gives the best overall fit to the present data.

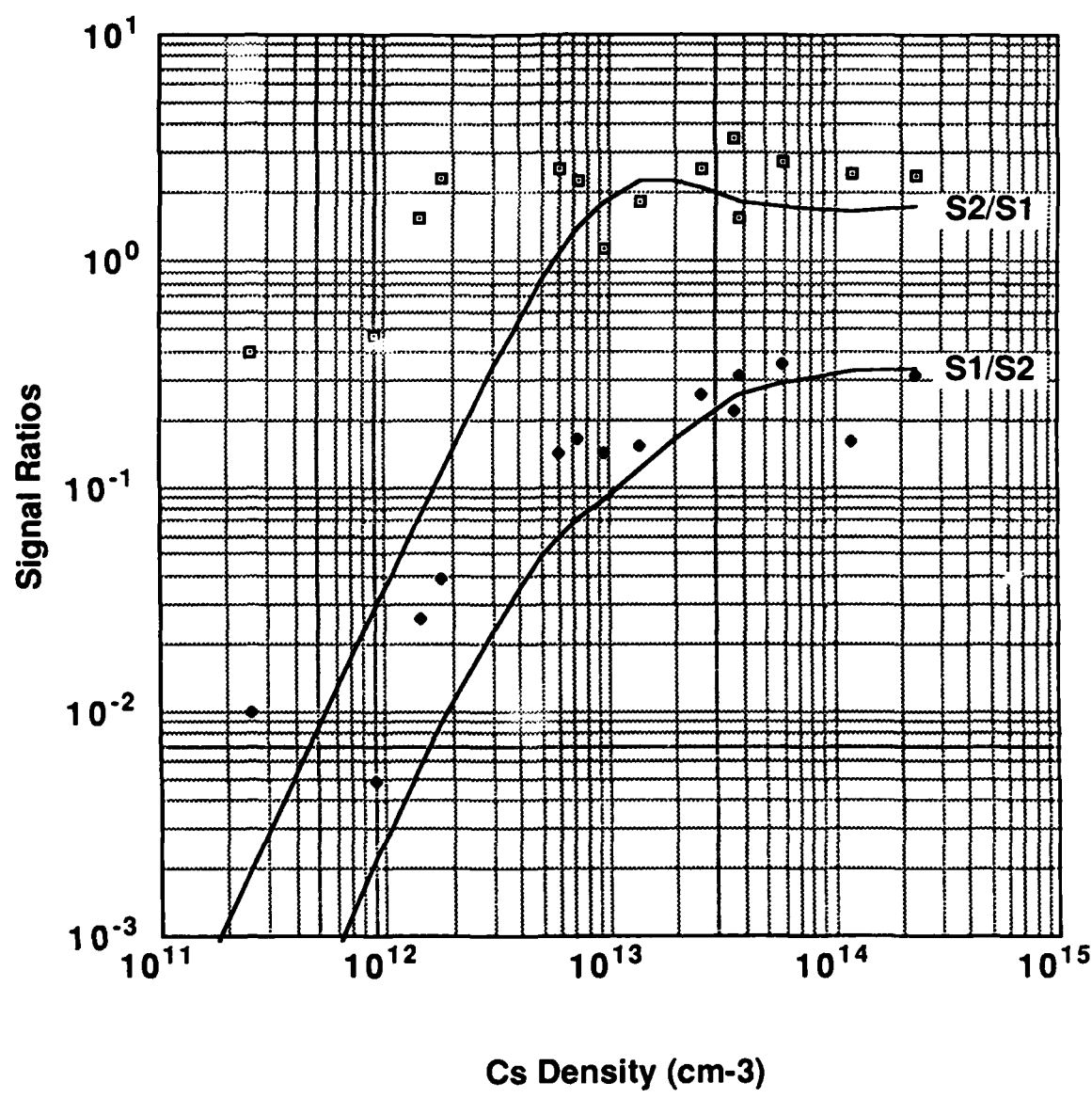


Figure 3.15 The ratio of the fluorescence signals at the instant  $t_p$  of the peak of the transferred signal. Subscripts 1 and 2 refer to the upper ( $6^2P_{3/2}$ ) and the lower ( $6^2P_{1/2}$ ) excited states respectively. Points are experimental data and the full curves are predictions of the model using  $\sigma_{12} = 1.3 \times 10^{-13} \text{ cm}^2$  and  $\sigma_{q1} = \sigma_{q2} = 2 \times 10^{-14} \text{ cm}^2$ .

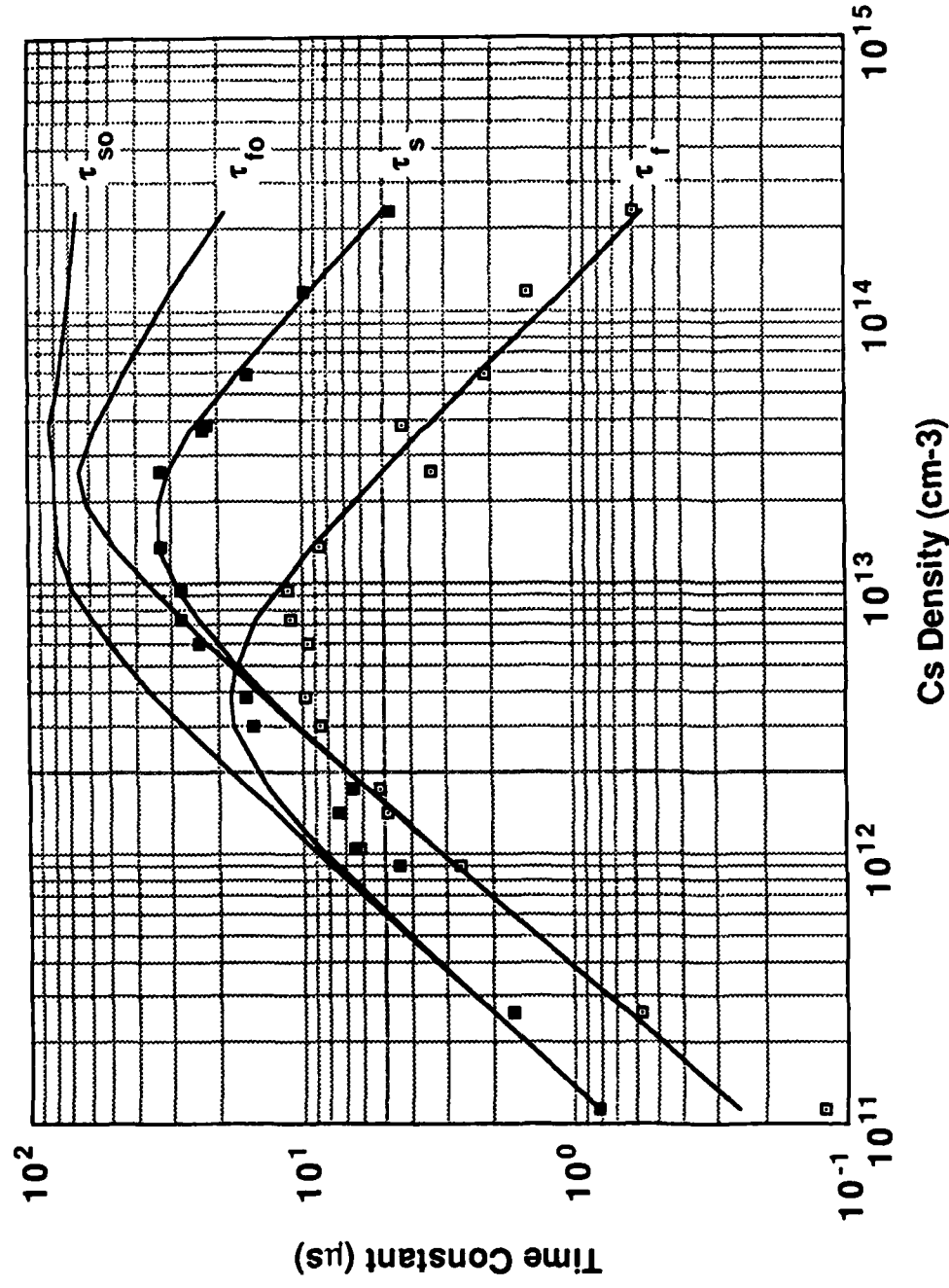


Figure 3.16 The fit of the collisional model using  $\sigma_{12} = 1.3 \times 10^{-13} \text{ cm}^2$  and  $\sigma_{q1} = \sigma_{q2} = 2 \times 10^{-14} \text{ cm}^2$ , shown by continuous curves, to the measured time constants, shown as points. Two sets of theoretical curves are shown: the upper curve in each case is the theoretical prediction of the behavior to be expected if the quenching cross section were zero.

A previous measurement of  $\sigma_{12}$  by Cjakowski and Krause (1965), performed at much lower densities where the effects of radiation trapping could be ignored, gave a value of  $3.1 \times 10^{-15} \text{ cm}^2$ . This value, together with  $\sigma_{q1} = 2 \times 10^{-13} \text{ cm}^2$  and  $\sigma_{q2} = 2 \times 10^{-14} \text{ cm}^2$ , provides an acceptable fit to the present  $\tau_f$  and  $\tau_s$  data, shown in Fig. 3.17. However, this set of cross sections fails significantly in fitting the signal ratio data, as shown in Fig. 3.18. Thus, we are forced to the conclusion that the value of  $\sigma_{12} = 3.1 \times 10^{-15} \text{ cm}^2$  is incompatible with the present measurements. No explanation for this discrepancy with the results of Cjakowski and Krause (1965) can be offered at this time.

For comparison purposes we also show in Figures 3.16 and 3.17 the behavior predicted for the case of zero quenching cross sections. The maximum value of  $\tau_s$  achieved in this situation, in the present size of container ( $R = 5.4 \text{ cm}$ ), would be  $83 \mu\text{s}$ , compared to  $35 \mu\text{s}$  achieved in the presence of the rather large quenching cross sections needed to account for the data.

### 3.5 PUMP POWER IMPLICATIONS

The conclusions drawn above regarding the achievable effective lifetime of the  $\text{Cs}^*(6^2\text{P})$  states allow us to make a firmer estimate than was previously possible of the pump power density likely to be needed in an optimized Cs-Tl ALF module. For example, assuming the module has the same size as the experimental tube used for the Cs fluorescence work reported above, and, as in the calculations of Section 2, that we need to sustain a  $\text{Tl}_m$  density of  $10^{10} \text{ cm}^{-3}$ , and that this would involve a corresponding density of  $4 \times 10^{10} \text{ cm}^{-3}$  of  $\text{Tl}_o$ , we can use Eq. (3.0) to calculate the dependence of  $[\text{Cs}^*]$  on  $[\text{Cs}_o]$ . The implied resonance line pump power density required to sustain the  $\text{Cs}^*$  is then calculated using  $\tau_{\text{eff}}$  appropriate to the value of  $[\text{Cs}_o]$ , read from  $\tau_s$  of Fig. 3.15. The resulting required pump power density has a minimum value of approximately  $6 \text{ mW/cm}^3$  in the region where  $[\text{Cs}_o] = 10^{13} \text{ cm}^{-3}$ , with a corresponding value of  $[\text{Cs}^*] = 8 \times 10^{11} \text{ cm}^{-3}$ . These densities of Cs and Tl are achievable simultaneously at a temperature close to  $400^\circ\text{C}$ .

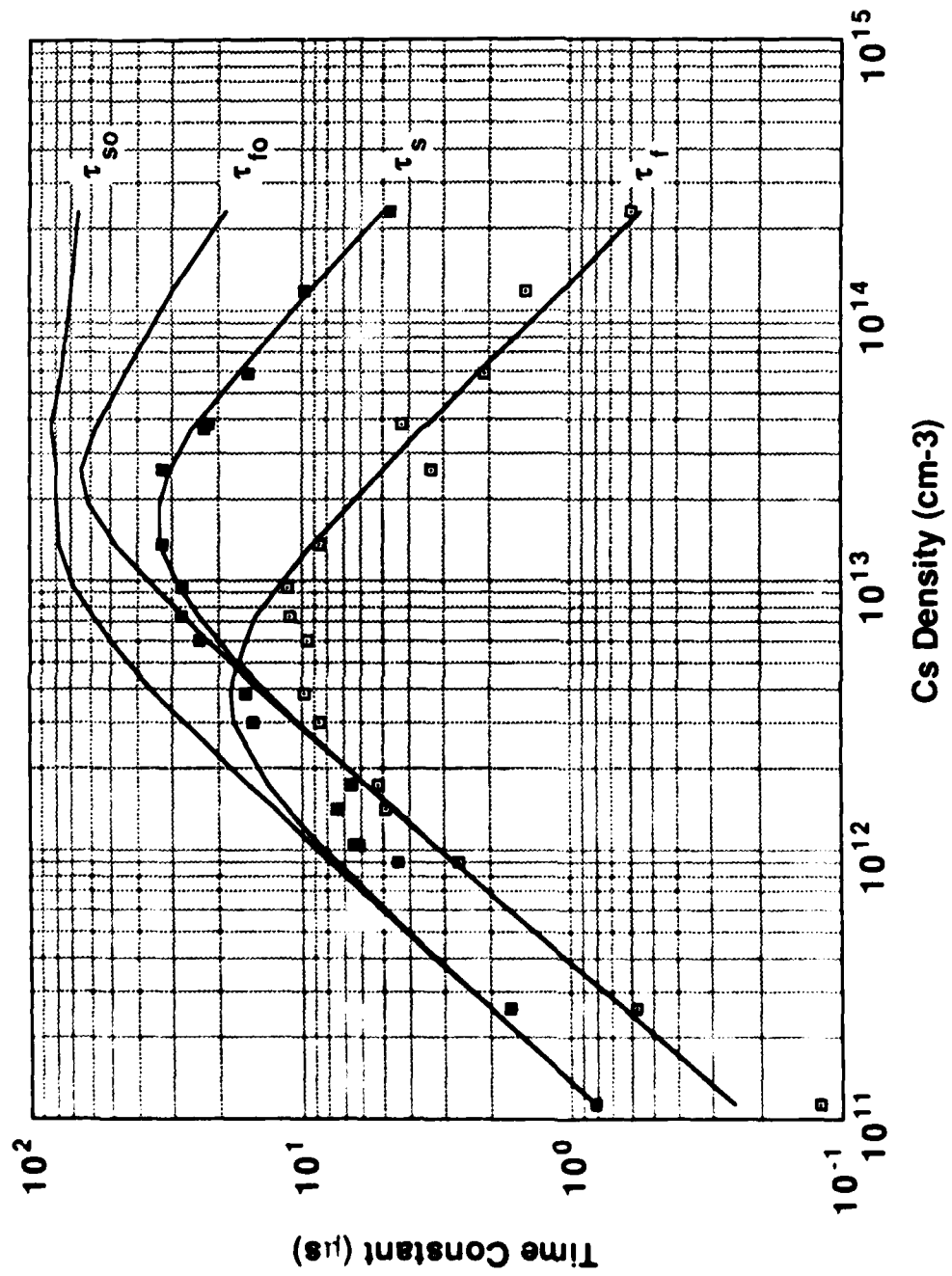


Figure 3.17 The same as Fig. 3.16, except that  $\sigma_{12} = 3.1 \times 10^{-15} \text{ cm}^2$ ,  $\sigma_{q1} = 2 \times 10^{-13} \text{ cm}^2$  and  $\sigma_{q2} = 2 \times 10^{-14} \text{ cm}^2$  have been used to compute the curves for  $\tau_s$  and  $\tau_f$ .

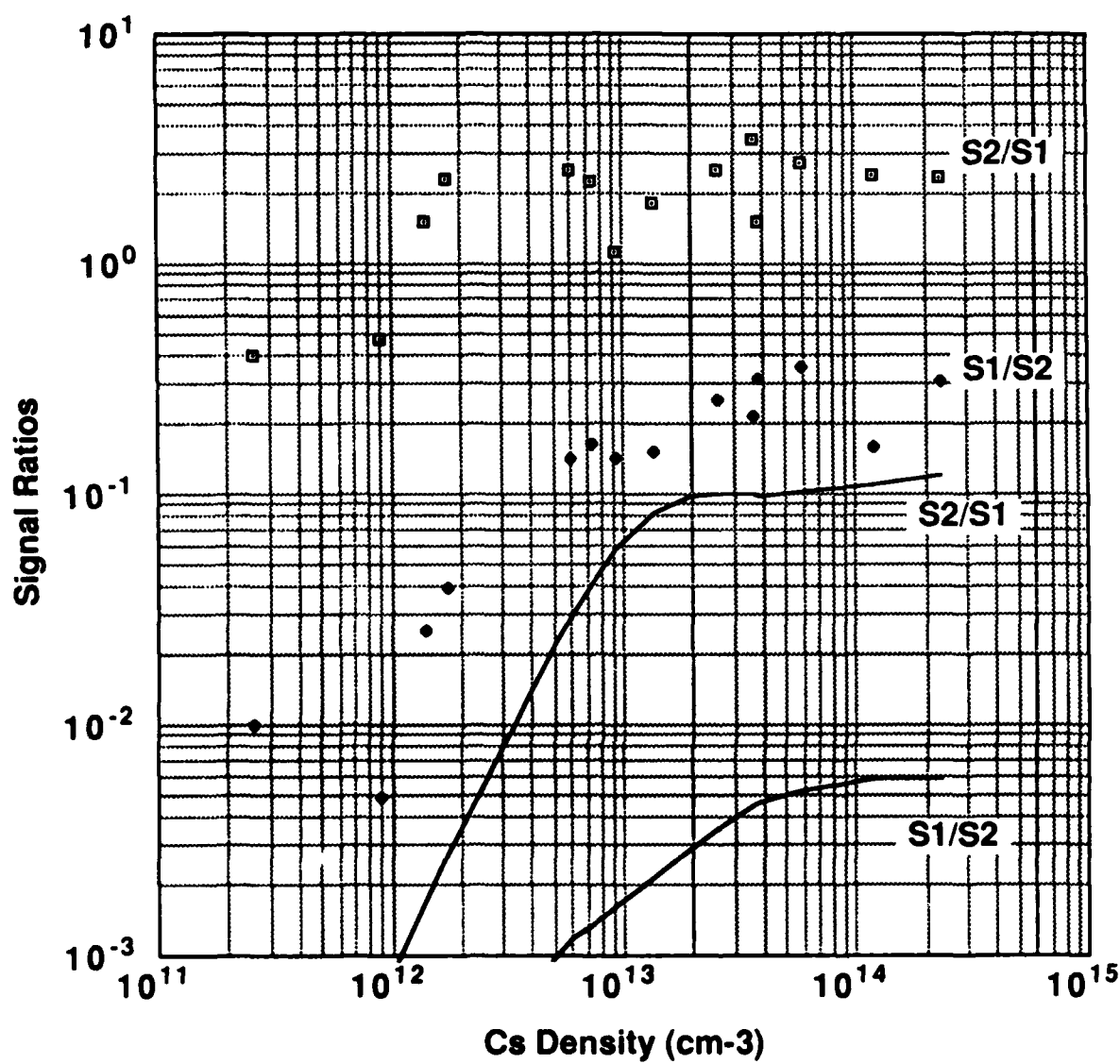


Figure 3.18 Same as Fig. 3.15 except that  $\sigma_{12} = 3.1 \times 10^{-15} \text{ cm}^2$ ,  $\sigma_{q1} = 2 \times 10^{-13} \text{ cm}^2$ , and  $\sigma_{q2} = 2 \times 10^{-14} \text{ cm}^2$  have been used to compute the full curves.

provided one uses an amalgam of the appropriate composition (Hirayama, 1986).

The above estimate applies to the locally absorbed pump power density, and therefore represents a lower bound on the resonance line power that would need to be applied to a given module. Because the medium is optically thick it will be desirable to employ a Cs resonance line source giving a suitably self-reversed profile, such that the module has an effective optical thickness of approximately unity. In this way it should be possible to efficiently pump the module more or less uniformly. Provided the pump line profile can be tailored in this way the actual supplied optical power would probably only need to be a factor of two or three greater than the lower bound obtained from the above calculation.

## 4. CONCLUSIONS AND RECOMMENDATIONS

In this section we present separately the conclusions and recommendations which follow from the work described in Section 2, concerning the TlCl based ALF concept, and from the work described in Section 3 which is pertinent to the Cs-Tl based ALF.

### 4.1 THE TlCl BASED ALF CONCEPT

The following conclusions are drawn from the sample calculations presented in Section 2:

1. There exists an extensive region of parameter space where a density of approximately  $1 \times 10^{10} \text{ cm}^{-3}$  of thallium metastables can be maintained by photodissociation of TlCl using pump power of approximately  $100 \text{ mW/cm}^2$ . The latter number is approximately inversely proportional to  $\sigma_1$ , the cross section for production of  $\text{Tl}_m$  by photodissociation of TlCl.
2. Mercury resonance line radiation at 254 nm is suitable for pumping this particular process.
3. The required densities of TlCl are sufficiently low, typically  $1 \times 10^{13} \text{ cm}^{-3}$ , that the system is optically thin to the pump radiation. This allows large volumes to be pumped uniformly without resorting to specially tailored pump line profiles or geometries.
4. The required container temperature has a lower bound of approximately  $250^\circ\text{C}$ , set by the prescribed density of TlCl, but a somewhat higher temperature may be necessary to avoid excessive coverage of the windows by condensed thallium.

The actual value could best be determined by experiment, but is not expected to exceed 400°C.

5. The density of  $Tl_o$  is conveniently controlled by the addition of excess chlorine to the mixture. An amount sufficient to give  $[Cl] \approx 1 \times 10^{15} \text{ cm}^{-3}$ , corresponding to  $[Cl_2] \approx 1 \times 10^{12} \text{ cm}^{-3}$ , is suitable for this purpose.
6. With the values assumed for the buffer gas quenching cross section ( $\sigma_g = 1 \times 10^{-19} \text{ cm}^2$ ) and the three body recombination rate coefficients ( $k_g = k_{10} = 1 \times 10^{-32} \text{ cm}^6/\text{s}$ ) a buffer gas cannot be added in sufficient amount ( $> 1 \times 10^{18} \text{ cm}^{-3}$ ) to usefully promote the volume recombination processes. Smaller amounts ( $[M] \approx 3 \times 10^{16} \text{ cm}^{-3}$ ) enhance the sustained density of metastables by inhibiting their transport to the walls, but at the expense of also increasing  $[Tl_o]$ .
7. Because of the direct sensitivity of the required pump power to the value of  $\sigma_1$  (the cross section for  $Tl_m$  production by photodissociation of  $TlCl$  at 254 nm) and in view of the uncertainties present in the literature regarding its value, an independent measurement of this quantity, and if possible of  $\sigma_2$  (the corresponding cross section for  $Tl_o$  production), would be very valuable.
8. This concept continues to appear viable, but proof-of-principle experiments using CW pumping are needed to better establish the required operating temperature and pump power.

#### 4.2 THE Cs-Tl BASED ALF CONCEPT

The following conclusions and recommendations are based on the work discussed in Section 3 of this report.

1. The measured effective lifetimes and relative fluorescence signals of the  $Cs(6^2P_{1/2})$  and  $Cs(6^2P_{3/2})$  in pure Cs vapor are consistent with lowest order mode radiation trapping

modified by collisional exchange of radiation between the states with an exothermic cross section of  $1.3 \times 10^{-13} \text{ cm}^2$ , and a self quenching cross section of  $2 \times 10^{-14} \text{ cm}^2$  of both states by ground state Cs.

2. The effect of the collisional self quenching is to define an optimum Cs density at which the effective lifetime maximizes, at  $\sim 35 \mu\text{s}$  in the present apparatus. In the absence of quenching a lifetime of  $83 \mu\text{s}$  could have been achieved. The lower value implies higher pump power than would otherwise be needed, but is nevertheless acceptable in the present context.
3. For a module of the same dimensions as the present experimental tube, operating at approximately  $400^\circ\text{C}$ , the required applied optical pump power would be approximately  $10-20 \text{ mW/cm}^3$  provided the pumping line profile and the Cs-Tl amalgam composition were both optimized.
4. A possible source of background noise in a Cs-Tl ALF is in-band radiation from higher lying Cs states, such as  $7^2\text{P}_{1/2,3/2} \rightarrow 6^2\text{S}_{1/2}$ , giving radiation at 459 and 455 nm respectively. The mechanism of excitation of such states would of necessity be a second order effect (Leslie et al., 1977), but the resulting signal might nevertheless be significant. The Cs cell used for the work described in Section 3 provides the opportunity to observe such radiation in pure Cs following resonance line pumping. Measurements of this type have been performed under another program, and will be reported in detail elsewhere (Liu et al., 1986). Based on the measured signal dependences on the Cs density, and on the pumping power density, the observed signals are ascribed to two-photon absorption of Cs<sub>0</sub> at the high instantaneous pump power densities used in the measurements. Under the low power CW pumping conditions prescribed for an actual ALF the resulting background is predicted to be negligibly small.

5. As the next major step in demonstrating the viability of a Cs-Tl ALF work is in progress using a Tl-Cs cell. The first objective, to observe the emission of 378 nm radiation resulting from the sequence of events represented in Figure 3.1, has recently been achieved. A detailed account of this work will be reported in detail elsewhere (Liu et al., 1986).
6. The remaining uncertainties in determining the viability of this concept are the cross sections appearing in Eq. (3.0). Of most importance is the ratio of  $\sigma_5/\sigma_2$ , a determination of which can best be made using a Cs-Tl cell in which the concentrations of  $Tl_o$ ,  $Tl_m$ ,  $Cs_o$ , and  $Cs^*$  can be individually monitored as a function of the optical pumping of the Cs. We plan to perform measurements of this type in the near future. Knowledge of all three cross sections,  $\sigma_{2,5,6}$ , for reactions 2, 5, and 6 in Table 3.1, is a prerequisite if confidence is to be placed in the design of a prototype ALF module.
7. Based on our best estimates of these unmeasured cross sections, we are unaware of any factor that would prevent the demonstration of a practical Tl-Cs ALF.

## 5. REFERENCES

Aleksandrov, E. B.; Baranov, A. V.; and Kulyasov, V. N. (1978). Opt. Spectrosc. (USSR), 44, 624-627.

Arimondo, E.; Inguscio, M.; and Violino, P. (1977). Revs. Mod. Phys. 49, 31-75.

Bellisio, J. A. and Davidovits, P. (1970). J. Chem. Phys. 53, 3474-3479.

Biberman, L. M. (1947). J. Exptl. Theoret. Phys. USSR, 17, 416 (Engl. Trans. ORNL-Tr-681).

Blickensderfer, R. P., Breckenridge, W. H., and Simons, J. (1976). J. Phys. Chem. 80, 653-659.

Brus, L. B. (1970). J. Chem. Phys. 52, 1716-1726.

Chantry, P. J. (1986). "A Simple Formula for Diffusion Calculations Involving Wall Reflection and Low Density," Submitted to J. Appl. Phys., 1986.

Chen, C. L. and Phelps, A. V. (1968). Phys. Rev. 173, 62-69.

Corliss, C. H. and Bosman, W. R. "Experimental Transition Probabilities for Spectral Lines of Seventy Elements," NBS Monograph 53, July 1962.

Cjakowski, M. and Krause, L. Can J. Phys. 43, 1259 (1965).

Csajkowski, M.; Skardis, G.; and Krause, L. Can J. Phys. 51, 334 (1973).

Davidovits, P. and Bellisio, J. A. (1971). J. Chem. Phys. 50, 3560-3567.

Gallagher, A. (1967). Phys. Rev. 157, 68.

Gedeon, A.; Edelstein, S. A.; and Davidovits, P. (1971). J. Chem. Phys. 55, 5171-5174.

Hirayama, C. (1986). Private communication. See C. S. Liu et al., 1986.

Holstein, T. (1947). *Phys. Rev.* 72, 1212-1233.

Holstein, T. (1951). *Phys. Rev.* 83, 1159-1168.

Huennekens, J. and Gallagher, A. (1983). *Phys. Rev. A* 28, 238-247.

Irons, F. E. (1979a). *J.Q.R.S.T.* 22, 1-20; (1979b) *J.Q.R.S.T.* 22, 21-36; (1979c) *J.Q.R.S.T.* 22, 37-44.

Leslie, S. G.; Verheyen, J. T.; and Millar, W. S. (1977). *J. Appl. Phys.* 48, 4444-4448.

Link, J. K. (1968). *J. Opt. Soc. Am.* 58, 1195.

Liu, C. S. (1985). Final Report to ONR Contract No. N00014-83-C-0416.

Liu, C. S.; Chen, C. L.; Chantry, P. J.; and Hirayama, C. (1986). Interim Report to Contract No. N00039-85-C-0080.

Maya, J. (1978). *Appl. Phys. Lett.* 32, 484-486.

Phelps, A. V. and McCoubrey, A. O. (1960). *Phys. Rev.* 118, 1561-1565.

Pickett, R. C. and Anderson, R. (1969). *J.Q.R.S.T.* 9, 697-704.

Rosser, W. A., Jr.; Wood, A. D.; and Gerry, E. T. (1969). *J. Chem. Phys.* 50, 4996-5008.

Scott, D. A. and Piper, J. A. (1986). *J. Chem. Phys.* 84, 4299-4303.

Stephenson, J. C. and Bradley Moore, C. (1972). *J. Chem. Phys.* 56, 1295-1308.

Taylor, J. B. and Langmuir, I. (1937). *Phys. Rev.* 51, 753.

VanVeen, N. J. A.; DeVries, M. S.; Baller, T.; and DeVries, A. E. (1981). *Chem. Phys.* 55, 371-381.

Walsh, P. J. (1959). *Phys. Rev.* 116, 511-515.

White, H. E. and Eliason, A. Y. (1933). *Phys. Rev.* 44, 753-756.

White, J. C. and Zdasink, G. A. (1978). *J. Chem. Phys.* 69, 2256-2257.

Yardley, J. T. (1980). "Introduction to Molecular Energy Transfer," Section 3.2, Academic Press, New York.

Zollweg, R. J.; Liebermann, R. W.; and McLain, D. K. (1981). *J. Appl. Phys.* 52, 3293-3303.

## ACKNOWLEDGEMENTS

We wish to thank Dr. M. B. White for originally suggesting the possibility of a thallium based ALP, for his subsequent contributions during many fruitful discussions, and for his continuing encouragement and support. We also thank our colleagues: Dr. I. Liberman for his continuing encouragement and helpful discussions, and Mr. W. Dooley for his high quality technical assistance. This report was typed by Mrs. M. B. Gross.